TOOLS

An *mTurq2-Col4a1* mouse model allows for live visualization of mammalian basement membrane development

Rebecca A. Jones[1], Brandon Trejo[1], Parijat Sil[1], Katherine A. Little[1], H. Amalia Pasolli[2], Bradley Joyce[1], Eszter Posfai[1], and Danelle Devenport[1]

Basement membranes (BMs) are specialized sheets of extracellular matrix that underlie epithelial and endothelial tissues. BMs regulate the traffic of cells and molecules between compartments, and participate in signaling, cell migration, and organogenesis. The dynamics of mammalian BMs, however, are poorly understood, largely due to a lack of models in which core BM components are endogenously labeled. Here, we describe the *mTurquoise2-Col4a1* mouse in which we fluorescently tag collagen IV, the main component of BMs. Using an innovative planar-sagittal live imaging technique to visualize the BM of developing skin, we directly observe BM deformation during hair follicle budding and basal progenitor cell divisions. The BM's inherent pliability enables dividing cells to remain attached to and deform the BM, rather than lose adhesion as generally thought. Using FRAP, we show BM collagen IV is extremely stable, even during periods of rapid epidermal growth. These findings demonstrate the utility of the *mTurq2-Col4a1* mouse to shed new light on mammalian BM developmental dynamics.

Introduction

The basement membrane (BM) is an ancient specialized extracellular matrix present in all metazoans (Özbek et al., 2010). It is a thin, dense sheet (~50–100 nm) that underlies all epithelial and endothelial tissues. The BM serves multiple functions, including structural support, maintenance of tissue integrity, and regulation of cell adhesion, migration, proliferation, and differentiation (Yurchenco, 2011). It is a complex structure composed of a network of proteins, glycoproteins, and proteoglycans and consists of three main layers: the lamina lucida, lamina densa (also called the basal lamina), and in some structures, the lamina fibro-reticularis (Timpl, 1996). Although it has been suggested that the lamina densa and lamina lucida subdivisions of the BM may be artifacts of conventional EM processing, it is more likely that these spatial compartments do exist but are masked by retention of soluble components in high-pressure freezing/freeze substitution EM sample preparation (Keene and Tufa, 2020). The lamina lucida is in direct contact with the basal surface of epithelial or endothelial cells and is made up primarily of laminins, nidogen, and other glycoproteins that are essential for cell adhesion and migration (Stanley et al., 1982; Schwarzbauer, 1999; Keene and Tufa, 2020; McGrath et al., 1994). The lamina densa, composed predominantly of type IV collagen, provides structural stability and acts as a barrier, separating the epithelial/endothelial compartment from the underlying mesenchyme (Pozzi et al., 2017; McGrath et al., 1994; Sauter et al., 1998).

Importantly, the BM acts as a selective filter, controlling the passage of cells and molecules between these different tissue compartments (Kelley et al., 2014). Many normal and pathological events involve cells transiting across BMs, including immune cell infiltration, cell migration during development, epithelial to mesenchymal transition, and cancer metastasis (Morrissey and Sherwood, 2015; Nakaya and Sheng, 2013; Micalizzi et al., 2010; Ratzinger et al., 2002). As well as acting as a selective barrier, BMs are essential for cell migration as they provide an active substrate to which cells can adhere. Laminins in BMs act as ligands to integrin receptors, coupling extracellular environmental cues to the actin cytoskeleton of cells (Hynes, 1992; Sekiguchi and Yamada, 2018b). In doing so, the BM also regulates cell behaviors. In terms of cell guidance, the BM is a reservoir of signaling cues and matrix molecules that guide many cell types along their migration path, including neurons during axonal pathfinding and neural crest-derived cells (Yasunaga et al., 2010; Leonard and Taneyhill, 2020;

....
[1]Department of Molecular Biology, Princeton University, Princeton, NJ, USA; [2]Electron Microscopy Resource Center, The Rockefeller University, New York, NY, USA.

Correspondence to Danelle Devenport: danelle@princeton.edu.

Banerjee et al., 2013). Tissue morphogenesis itself is regulated by BMs, via both molecular and biophysical processes. In the *Drosophila* embryo, the knockdown of collagen IV reduces adult wing size due to a reduction in BMP signaling (Ma et al., 2017), and heterogeneity of BM stiffness in *Drosophila* is important for egg elongation (Chlasta et al., 2017). Overall, the BM performs a wide variety of functions, including as a barrier, substrate, growth regulator, and signaling platform, from early development throughout the whole of adult life (Sherwood, 2021).

Studying BM dynamics or the crossing of cells through BMs in vivo is particularly challenging. BM crossing events are stochastic in nature and occur deep within tissues. Therefore, much of what is known about how cells cross BMs is derived from in vitro studies (Glentis et al., 2017; Bahr et al., 2022; Albini and Noonan, 2010), which, although informative, still require validation in the in vivo context. Our knowledge of the in vivo dynamics of BMs has come from elegant experiments in *Drosophila* and *Caenorhabditis elegans*, in which endogenous components of the BM have been fluorescently labeled. The *Vkg::GFP* (collagen IVa2) *Drosophila* line, created as part of a protein-trap strategy (Morin et al., 2001; Buszczak et al., 2007), has been invaluable in studying dissemination of tumor cells through the BM, as well as in BM-controlled shaping of growing organs during development (Tamori et al., 2016; Rei et al., 2021 *Preprint*; Harmansa et al., 2023; Page-McCaw et al., 2007; Page-McCaw, 2008). The stereotyped invasion of the *C. elegans* anchor cell through the uterine and vulval BMs during development, together with the successful endogenous tagging of over 60 *C. elegans* BM proteins has greatly increased our understanding of BM composition, dynamics, and the cellular and molecular mechanisms underpinning the invasion process (Schindler and Sherwood, 2013; Sherwood and Sternberg, 2003; Costa et al., 2023; Kelley et al., 2017, 2019; Keeley et al., 2020; Kenny-Ganzert and Sherwood, 2024).

A key bottleneck in our understanding of BM dynamics in mammals (and indeed vertebrates) is the inability to visualize the BM live, in vivo. Tagging endogenous BM components presents unique challenges because many are subject to extensive proteolytic cleavage and post-translational modifications (Frantz et al., 2010). Moreover, the addition of a fluorescent tag to a protein monomer that is subsequently highly crosslinked and integrated into a complex and dense protein network can interfere with the formation of that network via steric hindrance. Several attempts to visualize the vertebrate BM in vivo have been made, for example, the *lamC1:lamC1-sfGFP* zebrafish line recapitulates the reported mRNA expression pattern of endogenous *lamC1*, but the tag itself is not inserted into the endogenous genomic locus and the fusion protein is expressed as an additional copy (Yamaguchi et al., 2022; Sztal et al., 2011). Similarly, Futaki et al. (2023) have generated a *R26-CAG-Nid1-mCherry* mouse line in which the BM can be visualized in vivo; however, again this tag is not inserted in the endogenous locus; the fusion protein is expressed from a ubiquitous promoter that drives ectopic expression of Nid1-mCherry and causes reduced localization of endogenous Nid1. More recently, Morgner et al. (2023) generated an endogenous *Lamb1-Dendra2* mouse model in which heterozygous animals have fluorescently labeled laminin

β-1-containing BMs, which enabled tumor-cell mediated BM turnover to be measured using intravital microscopy. A limitation of this model, however, is that only BMs containing the laminin β-1 isoform can be visualized. In order to visualize all BMs and truly appreciate the structural complexity of the BM as a barrier, the ideal component to fluorescently tag is collagen IV, as it makes up ∼50% of all BMs (LeBleu et al., 2007).

Collagen IV is a heterotrimeric molecule, expressed ubiquitously in BMs, with all the collagen IV in mammals being derived from six different α-chains, encoded by the genes *COL4A1*, *COL4A2*, *COL4A3*, *COL4A4*, *COL4A5*, and *COL4A6* (Netzer et al., 1998; Mak and Mei, 2017). All BMs are composed solely of α1 and α2 chains during development, with some specialized structures adding a secondary network during maturation, such as α3/α4/α5 in the kidney glomerulus and α5/α5/α6 in mucosal epithelia (Kruegel and Miosge, 2010; Komori et al., 2018). Collagen IV is not required to initiate BM deposition during development, but the loss of both *Col4a1* and *Col4a2* is embryonically lethal in mice by E10.5 due to the lack of BM structural integrity and the breakdown of Reichert's membrane (Pöschl et al., 2004). As the α1 and α2 chains are ubiquitously expressed in BMs, we sought to label the endogenous *Col4a1* gene locus in mice to enable all BMs to be visualized.

In this work, we present the novel *mTurquoise2-Col4a1* (*mTurq2-Col4a1*) mouse line, in which endogenous collagen 4a1 (COL4A1), and therefore all BMs, are labeled. Despite being homozygous lethal, which is a developmental phenotype that requires further analysis, heterozygous animals are healthy and fertile, with normal BM architecture and composition in the dermal–epidermal junction BM of the skin, suggesting incorporation of the mTurquoise2 protein into one copy of endogenous *Col4a1* can support normal functionality of murine BMs. Furthermore, the stability and brightness of mTurquoise2 mean that BMs are clearly visible in heterozygous animals, allowing for long-term live imaging to be undertaken. Using an innovative mounting and imaging methodology, we show that the dermal–epidermal junction BM (hereafter referred to as the epidermal BM for simplicity) in embryonic mouse skin can be imaged long-term using explants from *mTurq2-Col4a1* mice. This has revealed new insights into epidermal BM morphology and behavior during hair follicle development, suggesting a previously underappreciated inherent pliability. Moreover, this flexibility of the epidermal BM allows dividing basal progenitor cells to maintain adhesion to the BM even during division, challenging the notion that all dividing cells reduce or lose their adhesion to the substrate when they round up in metaphase. We describe novel observations of COL4A1 in the dermis, including a potential role in stabilizing the developing dermal condensate. Finally, we show that despite the significant growth that occurs during E13.5 and E15.5, COL4A1 is strikingly stable in the BM of the developing epidermis, suggesting that the inherent pliability observed may be what allows for growth and morphogenetic changes rather than extensive proteolysis and degradation of the core components. We envisage that the *mTurq2-Col4a1* mouse model will be a useful addition to the field of BM research as it allows direct visualization of BM assembly, deformation and remodeling during development, and should be applicable to

Jones et al.
Live visualization of the murine basement membrane

Journal of Cell Biology   2 of 19
https://doi.org/10.1083/jcb.202309074

pathological conditions. Moreover, this model will allow many of the important observations made in vitro and in invertebrates to be visualized directly in the clinically relevant mouse model.

Results

Generation of the *mTurquoise2-Col4a1* mouse model

The collagen IV α chains are characterized by a central triple helical collagenous region of Gly-XY repeats, flanked by a 7S domain at the amino terminal and a globular NC1 carboxy domain (Fig. 1 A). The central collagenous region confers both structural stability and flexibility to the molecule, the NC1 domain is required to assemble the collagen α1α1α2(IV) heterotrimer, and the 7S domain is involved in the assembly of the formed heterotrimers into a more complex lattice network to form the BM (Timpl, 1989; Paulsson, 1992). It therefore follows that inserting a fluorescent protein in any position that interferes with or disrupts these domains may interfere with protein function and/or proper assembly of the BM. To inform our strategy, we studied the position of the *Drosophila Vkg::GFP* protein trap insertion, which is viable and labels all BMs (Morin et al., 2001; Buszczak et al., 2007). In this line, GFP is inserted between the N′ terminal signal sequence, which is cleaved within the cell before secretion, and the highly conserved 7S region. We mapped the *Vkg::GFP* insertion locus to the analogous position in the mouse *Col4a1* gene, which corresponds to a position toward the 5′ end of exon 2 (Fig. 1 B), specifically a target insertion site on the COL4A1 protein between amino acids K28 and G29.

Many fluorescent proteins, despite being termed monomeric, have a tendency to oligomerize under physiological conditions (Costantini et al., 2012). We therefore chose mTurquoise2 as our fluorescent protein tag as it does not homodimerize under any of the currently established gold-standard tests (Goedhart et al., 2012). mTurquoise2 also has an "in-built" linker region consisting of a short N′ terminal β-sheet juxtaposed away from the main β-barrel, which precludes the need for artificial linker sequences, which may be required for other fluorescent protein fusions such as mCherry (Goedhart et al., 2012). Moreover, mTurquoise2 has a low acid sensitivity (pKa 3.1), meaning it is stable in the lower pH of the lumenal and extracellular space (Denda et al., 2000; Chan and Mauro, 2011). It is also bright and photostable (t½ = 90 s compared with ∼50 s for EGFP), and its excitation/emission spectrum means it can be used in combination with YFP, mCherry/tdTomato, and other far-red fluorescent proteins (Lambert, 2019).

To insert the *mTurquoise2* ORF into the target locus of the *Col4a1* mouse gene, we used highly efficient two-cell homologous recombination CRISPR/Cas9-mediated mutagenesis as previously described (Gu et al., 2018, 2020). A circular plasmid repair template containing the *mTurquoise2* ORF flanked by ∼1,000 bp homology arms, together with a sgRNA and *Cas9* mRNA, was injected into the cytoplasm of both blastomeres of two-cell mouse embryos. Using this approach, we successfully generated an *mTurquoise2-collagen4a1* mouse line (*mTurq2-Col4a1*), in which the *mTurquoise2* ORF is inserted downstream of the cleaved signal sequence and upstream of the conserved 7S

domain (Fig. 1 B). Histological analysis of adult skin from *mTurq2-Col4a1/+* mice confirmed robust and clear localization of mTurq2-COL4A1 signal in the epidermal BM (Fig. 1, C–E and Fig. S1 A). In the kidney, mTurq2-COL4A1 signal was observed in Bowman's capsule, the mesangial matrix, and tubular BMs. (Fig. 1, F–I and Fig. S1 C). The mTurq2-COL4A1 signal in each tissue recapitulated the expression pattern of collagen IV antibody staining (Fig. 1, C", D", and G'). We also labeled both these tissues for perlecan, the most abundant heparan sulfate proteoglycan in the BM (Fig. 1, E, H, and I; and Fig. S1, B, E, and F). Aggregated perlecan connects the laminin polymers of the BM into the collagen IV network, in a "spot-welding" manner, thus connecting these two distinct and critical BM networks (Behrens et al., 2012). The pattern of mTurq2-COL4A1 expression coincided with perlecan expression in all BMs observed.

Characterization of mTurq2-COL4A1 expression in E18.5 mouse skin

The BM is established during embryonic development, with laminins expressed around gastrulation followed by collagen IV α1 and α2 chains shortly thereafter (Yurchenco et al., 2004). Studies have shown that although collagen IV is not required to initiate BM assembly, it is required for functional stabilization of BMs from as early as E10.5 (Guo et al., 1991; Guo and Kramer, 1989; Pöschl et al., 2004). Moreover, unlike laminins, which express additional subunit isoforms in post-natal life, collagen α1 and α2 chains are laid down mainly during embryogenesis, with only a small number of BMs replacing some of their α1 and α2 chains with α3/α4/α5 chains (Gunwar et al., 1998). We therefore examined the epidermal BM in embryonic mouse skin. Both WT and *mTurq2-Col4a1/+* embryos were labeled with antibodies against collagen IV (ColIV), laminin β-1 (Lamb1), and perlecan (Fig. 2). The epidermal BM was clearly labeled in *mTurq2-Col4a1/+* embryonic skin (Fig. 2, B‴ and E‴), and its localization overlapped with that of the ColIV antibody (Fig. 2 B").

The spatial relationship between the two major structural components of the BM, the lamina lucida and the lamina densa, is critical to BM function. The supramolecular laminin-containing network of the lamina lucida is linked to the collagen IV lamina densa network by the HSPG perlecan, with a potential role also played by agrin (Behrens et al., 2012; Hohenester and Yurchenco, 2013). In keeping with this, mutations in human *COL4A2* result in a failure of COL4A2 and laminin colocalization in the epidermal BM (Murray et al., 2014). Similarly, a 40% reduction in perlecan staining in all major BMs was observed in mice carrying *Col4a1* mutations (Jones et al., 2016). We, therefore, asked whether the relationships between these critical BM proteins are affected by the incorporation of mTurq2-COL4A1. To do so, we measured the linear correlation between Lamb1 and ColIV antibody labeling in WT and *mTurq2-Col4a1/+* E18.5 epidermal BMs at pixel-level scale in high-resolution images (see Materials and methods). As expected, we saw that the Pearson's Correlation Coefficient (PCC) r value was variable, as both supramolecular networks will not occupy the same space, but crucially, no difference was detected between WT and *mTurq2-Col4a1/+* backskins, suggesting that the
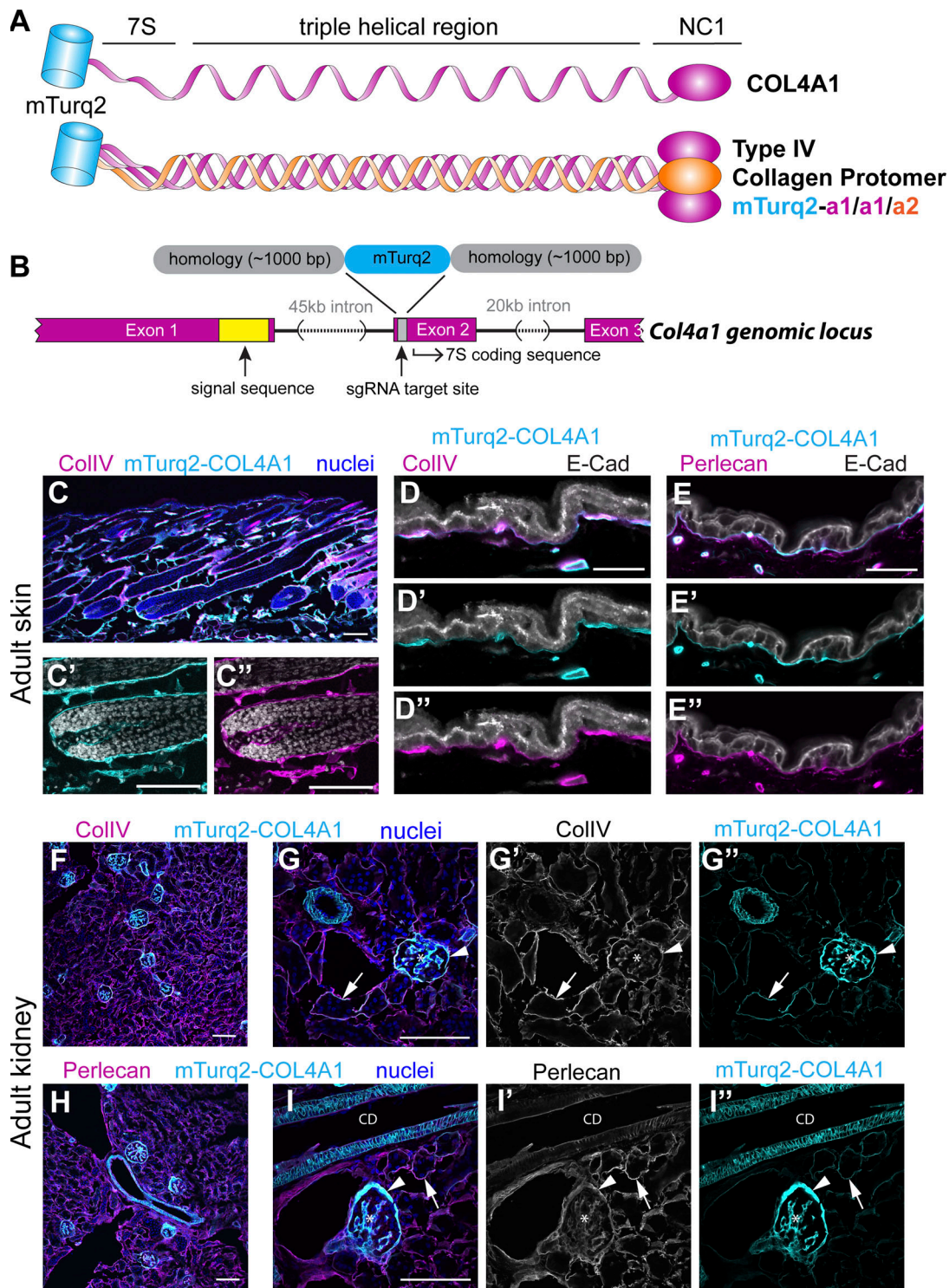
Jones et al.
Live visualization of the murine basement membrane

Journal of Cell Biology   3 of 19
https://doi.org/10.1083/jcb.202309074

Figure 1. ***mTurq2-Col4a1* endogenously tagged reporter design and basement membrane localization in adult mouse tissues. (A)** Schematic of the COL4A1 subunit and type IV collagen trimeric protomer with an N-terminal mTurq2 fluorescent tag. **(B)** Schematic of the *Mus musculus Col4a1* genomic locus and *mTurq2* insertion site. The *mTurq2* gene was inserted into Exon 2 between the coding sequences for the signal peptide and 7S domain. **(C)** Sagittal section of dorsal skin from *mTurq2-Col4a1/+* adult mouse labeled with ColIV antibodies (magenta) and Hoechst to mark nuclei (blue; grayscale in C' and C''). **(C')** mTurq2-COL4A1 (cyan) localizes to BM surrounding the hair follicle, where it overlaps with ColIV staining (C'', magenta). Scale bars, 100 µm. **(D–D'')** High magnification view of mTurq2-COL4A1 (cyan) localization in the interfollicular epidermis from *mTurq2-Col4a1/+* adult mouse labeled with ColIV (magenta) and E-Cadherin (E-Cad; grayscale). Scale bar, 20 µm. **(E–E'')** High magnification view of mTurq2-COL4A1 (cyan) localization in the interfollicular epidermis from *mTurq2-Col4a1/+* adult mouse labeled with Perlecan (magenta) and E-Cadherin (E-Cad; grayscale). Scale bar, 20 µm. **(F)** Kidney section from *mTurq2-Col4a1/+* adult mouse labeled with ColIV (magenta) and Hoechst to mark nuclei (blue). Scale bar, 100 µm. **(G–G'')** High magnification view of mTurq2-COL4A1 (cyan) localization in the kidney of *mTurq2-Col4a1/+* adult mouse labeled with ColIV (magenta in G; grayscale in G') Hoechst (blue). mTurq2-COL4A1 expression can be seen in renal tubules (arrows), Bowman's capsule (arrowheads), and the mesangial matrix (asterisks). Scale bar, 100 µm. **(H)** Kidney section from *mTurq2-*

Col4a1/+ adult mouse labeled with Perlecan (magenta) and Hoechst (blue). Scale bar, 100 µm. **(I–I'')** High magnification view of mTurq2-COL4A1 (cyan) localization in the kidney of *mTurq2-Col4a1/+* adult mouse labeled with Perlecan (magenta in G; grayscale in G') and Hoechst (blue). mTurq2-COL4A1 expression can be seen in renal tubules (arrows), Bowman's capsule (arrowheads), the mesangial matrix (asterisks), and the collecting duct (CD). Scale bar, 100 µm.

---

mTurq2-Col4a1/+ allele does not interfere with the network interactions of laminin β-1 and collagen IV (Fig. 2 C). We repeated this analysis measuring the correlation between Lamb1 and perlecan antibody labeling and observed that the perlecan localization profile in *mTurq2-Col4a1/+* E18.5 epidermal BMs resembled that of WT littermates (Fig. 2, D'', E'', and F). Taken together, these data demonstrate that the structure of the epidermal BM in *mTurq-Col4a1/+* embryos resembles that of WT littermates.
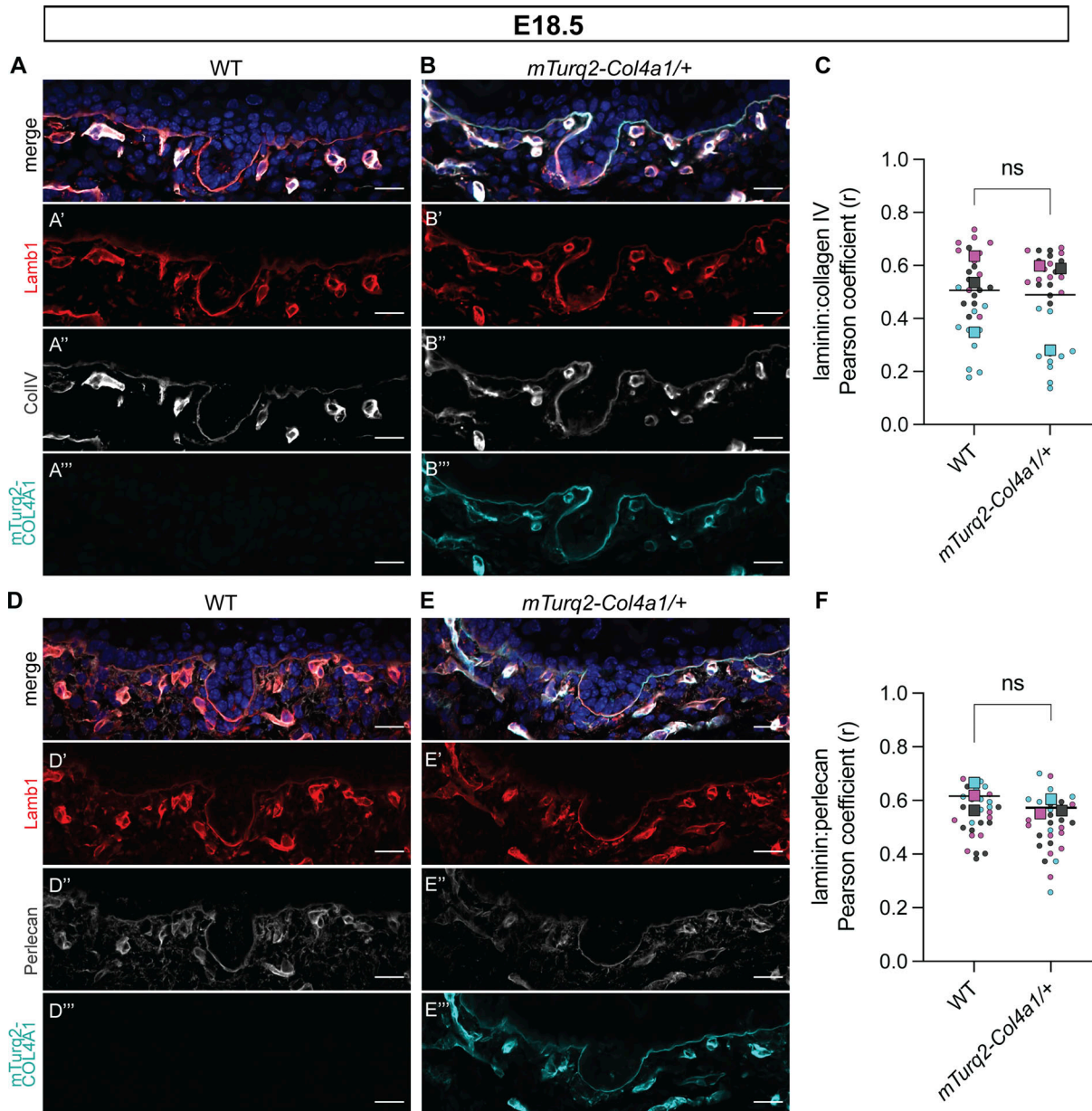
Figure 2. **E18.5 *mTurq2-Col4a1* mouse backskin shows correct and robust expression of mTurq2-COL4A1 in the dermal–epidermal junction basement membrane. (A)** Average intensity projection of backskin from WT E18.5 embryo labeled with Hoechst (merge, top), anti-laminin β-1 antibody (A'), and anti-collagen IV antibody (A''). No signal was observed in the mTurq2 channel (A'''). **(B)** As in A, except backskin from a *mTurq2-Col4a1/+* embryo. Robust mTurquoise2 signal recapitulates the labeling pattern of the collagen IV antibody. **(C)** Pearson's correlation coefficient (r) measuring the correlation between laminin β-1 and collagen IV expression (antibody labeling) in WT and *mTurq2-Col4a1/+* E18.5 backskins as labeled. Larger datapoints—biological replicates (n = 3 embryos), smaller datapoints—individual images per replicate (n = 10 per embryo). **(D)** Average intensity projection of backskin from WT E18.5 embryo labeled with Hoechst (merge, top), anti-laminin β-1 antibody (D'), and anti-perlecan antibody (D''). **(E)** As in D, except backskin from a *mTurq2-Col4a1/+* embryo. **(F)** As in C, except measuring the correlation between laminin β-1 and perlecan. Scale bar, 20 µm. ns = not significant, Mann–Whitney *U* test.

Despite numerous (>10) heterozygous crosses at several stages during development of the *mTurq2-Col4a1* line, we never observed the birth of any homozygous pups. This suggests that the *mTurq2-Col4a1* line is embryonically homozygous lethal, although we saw no apparent defects in heterozygous mice, which resemble WT littermates in terms of longevity, fertility, and overall health. The fact that heterozygous animals were viable, healthy, and fertile suggested that incorporation of the mTurq2-COL4A1 protein was not overtly deleterious to BM function when present as a single genomic copy. Furthermore, our correlation coefficient data in skin showed no difference in the spatial relationships between core BM components, as would be expected if incorporation of the mTurq2-COL4A1 protomer was detrimental to BM formation. However, despite attaining high-resolution images to complete this analysis, our data were inherently limited by the resolution limits of light microscopy. To study the BM of *mTurq2-Col4a1/+* epidermis at the ultrastructural level, therefore, we next turned to electron microscopy.

Basement membranes in *mTurq2-Col4a1/+* mice resemble those of WT littermates at the ultrastructural level

Using transmission electron microscopy (TEM), we performed a detailed analysis of skin architecture and the BM at the dermal–epidermal junction of E18.5 *mTurq2-Col4a1/+* embryos (Fig. 3). The overall skin architecture in *mTurq2-Col4a1/+* embryos was similar to WT littermates, consisting of five distinct layers (dermis, basal, spinous, granular, and stratum corneum) that displayed characteristic morphologies associated with each layer (i.e., dense keratin bundles in the spinous layer and keratohyalin granules in the granular layer; Fig. 3, A and B; and Fig. S2). High magnification views of the junction between the basal epithelial layer and the underlying dermis showed numerous and regularly spaced BM thickenings at sites of hemidesmosome attachments (Fig. 3, C–F and Fig. S2). These electron-dense sites of dermal–epidermal adhesion consisted of inner and outer hemidesmosome plaques associated with intracellular keratin intermediate filaments (Fig. 3, G and H; and Fig. S2). Beneath the plasma membrane of basal epidermal cells, the lamina lucida and lamina densa layers of the BM were each clearly distinguishable. Furthermore, the thickness of the lamina densa, where type IV collagen accumulates, was comparable between the skins of *mTurq2-Col4a1/+* and their WT littermates (Fig. 3, G and H; and Fig. S2). Thus, at the ultrastructural level, the skin of *mTurq2-Col4a1/+* embryos displayed all the hallmarks of normal dermal–epidermal junction assembly.

Characterization of mTurq2-COL4A1 expression in earlier embryonic stages

Having shown that our *mTurq2-Col4a1/+* mice display robust mTurq2-COL4A1 signal in both adult and late embryonic stage skin, we now sought to characterize the distribution of *mTurq2-COL4A1* during BM assembly and maturation in earlier embryonic stages. To do this, we harvested embryos at E15.5 and labeled the backskins of both WT and *mTurq2-Col4a1/+* embryos with antibodies against laminin β-1 (Lamb1), collagen IV (ColIV), and perlecan (Fig. 4). XZ optical reconstructions of Z stack images of E15.5 skins clearly show robust mTurq2-COL4A1 signal in

the epidermal BM of both the IFE and developing hair follicles that recapitulates the ColIV antibody labeling (Fig. 4 B). As described above, we then calculated the PCC of the spatial relationship between Lamb1 and ColIV antibody labeling in both WT and *mTurq2-Col4a1/+* E15.5 epidermal BMs (Fig. 4, A and B) and detected no difference between the genotypes (Fig. 4 C), further validating our previous findings that incorporation of mTurq2-COL4A1 into the epidermal BM does not alter the interaction between these two supramolecular layers, at least in the skin.

To take this analysis further, we next measured how much of the laminin β-1 localization domain within the epidermal BM overlaps with that of the collagen IV localization domain. We analyzed high-resolution images of the epidermal BM from both WT and *mTurq2-Col4a1/+* backskins and applied a custom FIJI macro to calculate the fraction of each protein that overlaps with the other (overlap fraction; see Materials and methods). Our results demonstrate that a higher fraction of collagen IV (~70%) is found to overlap with laminin β-1 localization at E15.5 (Fig. 4 E). Laminin β-1 is more frequently observed not colocalizing with collagen IV (<50% overlap; Fig. 4 D). Crucially, we observed no difference between the overlap fractions of laminin β-1 and collagen IV in WT and *mTurq2-Col4a1/+* backskins (Fig. 4, D and E). We repeated these analyses with the laminin β-1 and perlecan localization domains (Fig. 4, H–J). Here, we observed a similar contribution to the area of colocalization by both laminin β-1 and perlecan (Fig. 4, I and J), and again we saw no difference between WT and *mTurq2-Col4a1/+* in either analysis. As these results reflected what we observed in E18.5 embryos, we expanded our analysis to E12.5 embryos, a developmental time prior to both hair follicle development and stratification, when the basal progenitor layer is one-cell thick (Fig. 4, K–Q). We hypothesized that due to the significant growth of the embryo and expansion of the skin between these stages, the epidermal BM morphology and overlap composition would differ in E12.5 embryos. Again, we observed well-defined labeling of the epidermal BM with mTurq2-COL4A1 that recapitulated ColIV antibody labeling (Fig. 4, K–L) and detected no differences in the spatial relationships between laminin β-1 and collagen IV/perlecan in E12.5 WT and *mTurq2-Col4a1/+* BMs, respectively (Fig. 4, K–O and P–T). Surprisingly, we observed very similar overlap fractions of laminin β-1 and collagen IV/perlecan in E12.5 compared with E15.5. This suggests that the morphology and composition of the epidermal BM, with respect to these core components, does not change significantly over time and is established during the early stages of embryonic skin development.

Live imaging of *mTurq2-Col4a1/+* backskins by a Planar-Sagittal (PS) Multiview imaging approach reveals new insights into developmental BM dynamics

Having shown that the *mTurq2-Col4a1* mouse model faithfully labels the epidermal BM, we next explored its utility for live imaging developmental BM dynamics. As the epidermal BM has a thickness of around 100 nm and developing mouse skin is inherently undulating, to properly visualize BM dynamics, a sagittal view of developing skin explants is necessary. Established live imaging approaches obtain planar XY images and the
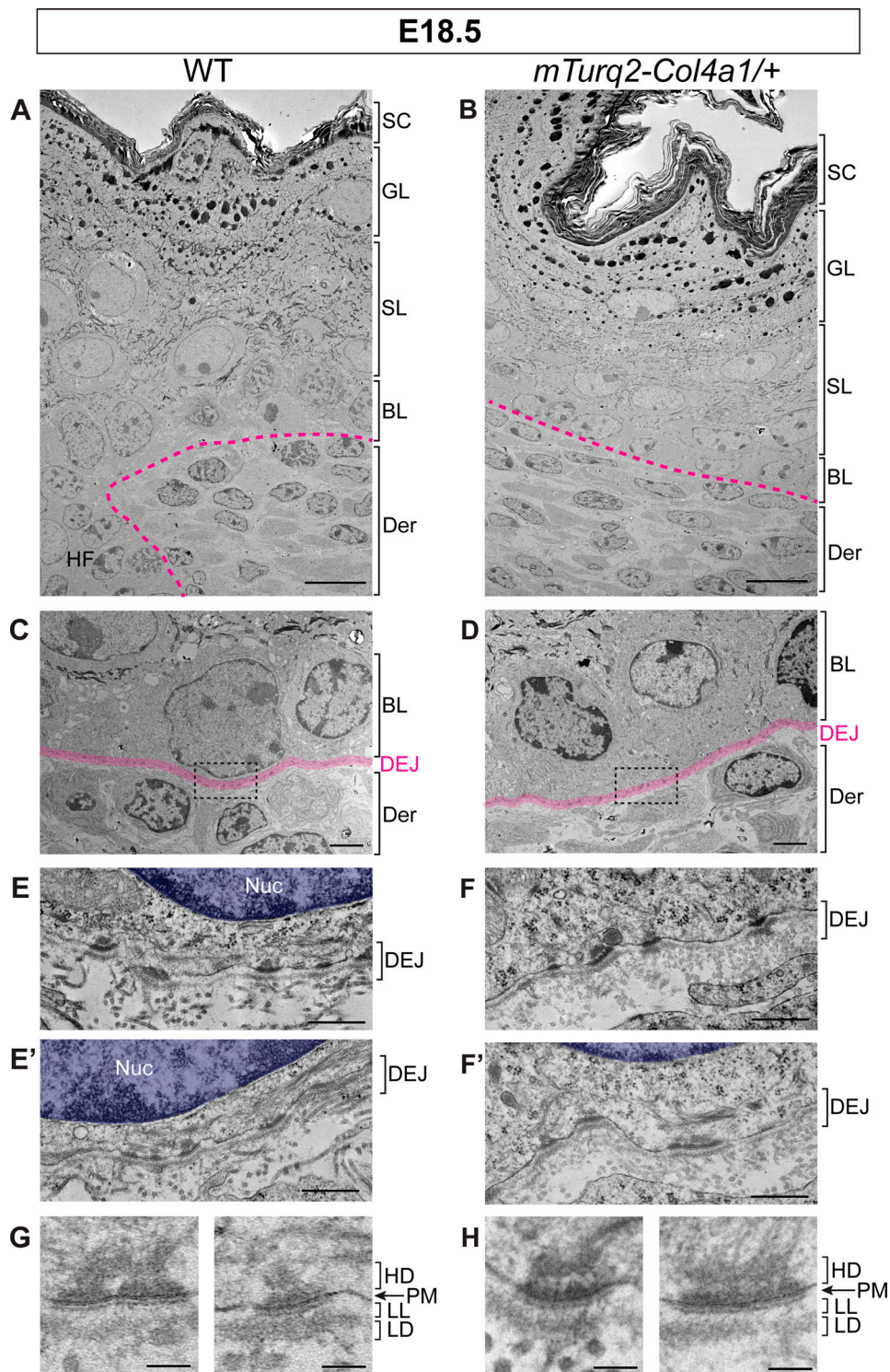
Jones et al.
Live visualization of the murine basement membrane

Journal of Cell Biology   6 of 19
https://doi.org/10.1083/jcb.202309074

Figure 3. Normal ultrastructural organization of the epidermis and dermal-epidermal junction in *mTurq2-Col4a1/+* embryonic skin. Transmission electron micrographs of ultrathin skin sections from E18.5 WT control (A, C, E, and G) and *mTurq2-Col4a1/+* (B, D, F, and H) embryos. **(A and B)** Ultrastructural overview of skin architecture. Der = dermis, BL = basal layer, SL = spinous layer, GL = granular layer, SC = stratum corneum, HF = hair follicle. The dotted line denotes dermal–epidermal boundary. Scale bars, 10 µm. **(C and D)** Zoomed in view of the boundary between the basal epithelial layer and dermis. Dermal–epidermal junction (DEJ) is highlighted in pink. Dotted boxes denote regions magnified in E and F. Scale bars, 2 µm. **(E and F)** Two representative examples of DEJ region of the skin from WT (E and E') and *mTurq2-Col4a1/+* (F and F') embryos. Nuc = nucleus. Scale bars, 500 nm. **(G and H)** Zoomed in views of individual hemidesmosomes at the DEJ. HD = hemidesmosome, PM = plasma membrane, LL = lamina lucida, LD = lamina densa. Scale bars, 100 nm.

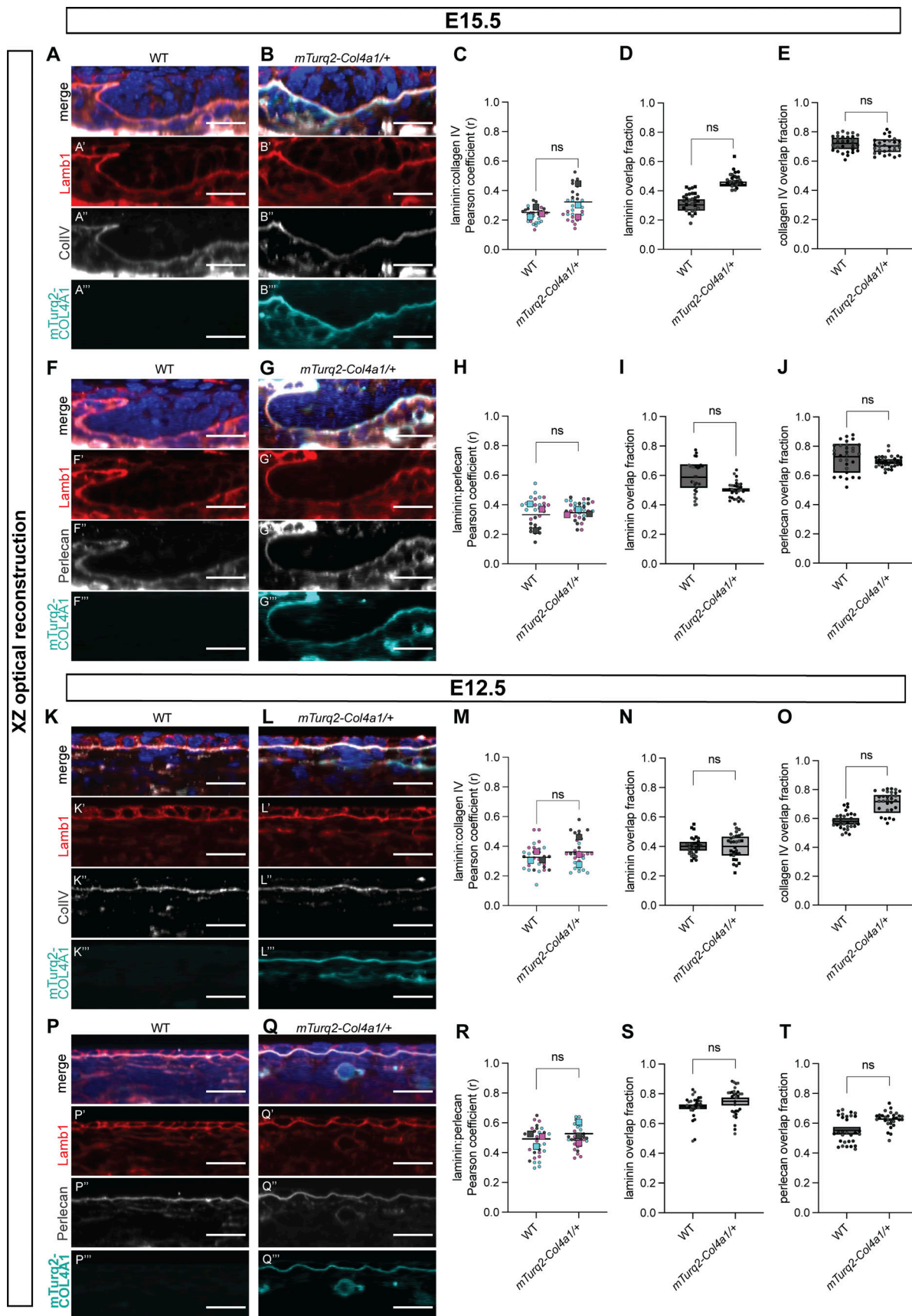**Figure 4. Spatial distribution and correlation between key basement membrane components in *mTurq2-Col4a1/+* embryonic backskins resembles that of WT littermates. (A)** Average intensity projection (XZ optical reconstruction) of backskin from WT E15.5 embryo labeled with Hoechst (merge, top),

Jones et al.
Live visualization of the murine basement membrane

Journal of Cell Biology   8 of 19
https://doi.org/10.1083/jcb.202309074

anti-laminin β-1 antibody (A'), and anti-collagen IV antibody (A''). No signal is observed in the mTurq2 channel (A'''). **(B)** As in A, except backskin from a *mTurq2-Col4a1/+* embryo. Robust mTurq2-COL4A1 signal recapitulates the labeling pattern of the collagen IV antibody. **(C)** Pearson's correlation coefficient (r) measuring the correlation between laminin β-1 and collagen IV expression (antibody labeling) in WT and *mTurq2-Col4a1/+* E15.5 backskins as labeled. Larger datapoints—biological replicate means (n = 3 embryos), smaller datapoints—individual images per replicate (n = 10 per embryo). **(D)** Fraction of laminin β-1 contribution to the laminin β-1:collagen IV overlap in E15.5 backskins; refer to the main text for methodology. **(E)** As in D, except collagen IV contribution to laminin β-1:collagen IV overlap. Dots represent individual images (n = 10 per embryo) and boxes denote the minimum and maximum mean per biological replicate (n = 3 embryos). **(F)** Average intensity projection (XZ optical reconstruction) of backskin from WT E15.5 embryo labeled with Hoechst (merge, top), anti-laminin β-1 antibody (F'), and anti-perlecan antibody (F''). **(G)** As in F, except backskin from an *mTurq2-Col4a1/+* embryo. **(H–J)** As in C–E, except measuring the correlation and overlap fractions between laminin β-1 and perlecan. **(K–T)** As in A–J, except backskins are from E12.5 embryos. Scale bars, 20 μm. ns = not significant, Mann–Whitney *U* test.

---

sagittal view is reconstructed from the Z-stack (Fig. 5 A). However, Abbe's formula (lateral (XY) resolution = $\lambda/2NA$ and axial (Z) resolution = $2\lambda/NA^2$) states that lateral resolution will always be greater than axial resolution in both widefield and confocal microscopy (Huszka and Gijs, 2019), so obtaining a high-resolution sagittal image is a limitation of this method. To image the epidermal BM in all three dimensions with a similar resolution and without the need for software reconstruction, we developed a novel live imaging technique, PS Multiview imaging. This simple technique involves folding the skin explant over an agarose ridge allowing the focal plane to be set at either the standard planar imaging plane (XY) or the sagittal imaging plane ("XZ"; Fig. 5 B and Video 1). This sagittal view of the developing skin allows for high-resolution imaging of cells and tissues in "Z," without the need for reconstruction. By combining PS Multiview imaging with *mTurq2-Col4a1/+* backskins in which all cell membranes are labeled with tdTomato (*mTmG/mTmG*), we were able to long-term live image the epidermal BM in developing skin explants (Fig. 5 C and Video 1).

As we were able to long-term live image the developing epidermal BM, we next wanted to visualize BM dynamics during the morphogenesis of hair follicles, which involves an initially thickened placode of basal epidermal cells that buds into the underlying dermis. The BM has been shown to play both an active and passive role during tissue development (Walma and Yamada, 2020) and is thought to be extensively remodeled during epithelial morphogenesis. For example, during branching morphogenesis, the BM surrounding actively growing branch tips becomes thin and/or discontinuous with microperforations, which is thought to allow for tip expansion and branch elongation (Harunaga et al., 2014; Spurlin et al., 2019; Sekiguchi and Yamada, 2018a). Given the wide-ranging roles of the BM during morphogenesis, we sought to investigate BM dynamics during hair follicle budding by live imaging E14.5–E15.5 *mTurq2-Col4a1/+;mTmG/mTmG* backskins over several hours using PS Multiview imaging (Fig. 5 C and Video 1).

We used the fluorescence intensity of the mTurq2-COL4A1 signal as a read-out for changes to the epidermal BM under an invaginating hair follicle relative to the neighboring IFE that is not undergoing significant morphological changes (Fig. 5 D). Surprisingly, the mTurq2-COL4A1 signal intensity was significantly greater at the actively growing base of developing hair follicles than at the IFE (Fig. 5 E). Although we had expected the intensity to become fainter, more diffuse, or discontinuous as downward budding occurred, the signal became brighter and qualitatively more uniform in appearance. This suggested that

the epidermal BM may be compressed by the epithelium during hair follicle invagination or that new mTurq2-COL4A1 incorporation exceeds proteolytic degradation during budding, unlike in other examples of budding/branching morphogenesis (Wang et al., 2017; Sekiguchi and Yamada, 2018a).

Another cellular force that acts upon the epidermal BM is cell division. Several studies have shown that when cells in culture approach mitosis, they detach from the ECM and disassemble their adhesions to retract from the matrix and round up in metaphase (Champion et al., 2017; Suzuki and Takahashi, 2003; Yamakita et al., 1999). U2OS cells have been shown to use reticular adhesions to mediate substrate attachment during mitosis due to the complete disassembly of focal adhesions (Lock et al., 2018). Similarly, epithelial cells are thought to reduce or lose their adhesions to the BM when undergoing division, and this breakdown of focal adhesions during mitosis has been shown to be important for macrophage infiltration in *Drosophila* (Matus et al., 2014; Jones et al., 2019; Akhmanova et al., 2022). Since basal cells within the epidermis divide frequently during development (Damen et al., 2021; Box et al., 2019), we wanted to examine the interface between dividing basal cells and the epidermal BM. We analyzed several movies in which numerous basal cells were seen to go from interphase through to complete cytokinesis, and, to our surprise, we observed that when dividing cells rounded up in metaphase, they did not detach from the epidermal BM (Fig. 5 F; and Fig. S3, A and B; Video 2). Instead, rounded cells remained closely adhered to the BM, which subsequently deformed around the base of the dividing cell. To quantify this BM deformation, we measured the angle of the BM at the junction between the dividing cell and its neighbors before, during, and after mitosis (interphase, metaphase, and cytokinesis, respectively). We found that the epidermal BM pinches inward by an average of 25° underneath a rounded dividing cell and then reverts to the near-straight interphase angle after division, implicating maintained adhesion to the BM throughout mitosis (Fig. 5 G and Fig. S3 C). Antibody labeling for integrin β4, the laminin receptor essential for cell-BM hemidesmosomes, showed that dividing cells maintain integrin β4–mediated adhesions during mitosis (Fig. S3, D–G). Moreover, TEM analysis of dividing cells revealed hemidesmosome attachments are not only maintained during rounding but appear unchanged from those in non-dividing cells (Fig. S3, H–J and Fig. 3). Taken together, these data show that dividing basal progenitor cells do not disassemble hemidesmosome adhesions to the BM during division. In keeping with our previous observations of epidermal BM deformation underneath
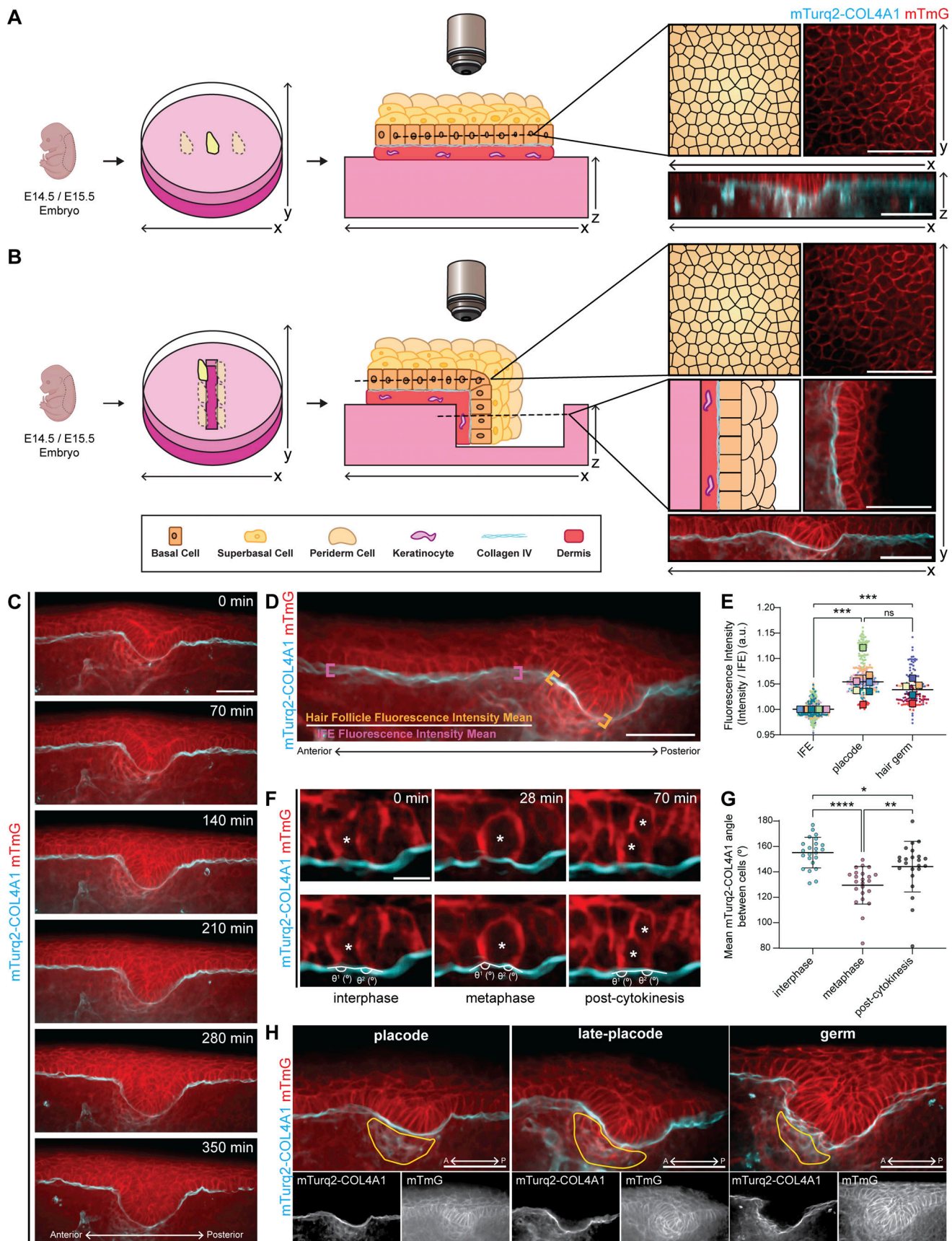
Figure 5. **PS Multiview imaging of *mTurq2-Col4a1* mouse model. (A)** Schematic of established live imaging method. The skin explant is mounted on an agarose pad and imaged using spinning disc microscopy. To visualize the tissue in Z, the image is software-reconstructed. Scale bar, 50 µm. **(B)** Schematic of PS

Multiview live imaging. The skin explant is mounted as previous, but over an agarose ridge. Both planar (XY) and sagittal ("XZ") focal planes are then imaged. Scale bar, 50 μm. **(C)** Snapshots taken from a time-lapse live imaging movie of hair follicle invagination in E14.5 *mTurq2-Col4a1/+;mTmG/mTmG* backskin. **(D)** Representative image showing mean fluorescence intensity calculation methodology. Orange brackets highlight the hair follicle base region where signal intensity was measured. Magenta brackets highlight the IFE region where the signal intensity was measured. Scale bar, 50 μm. **(E)** Quantification of mTurq2-COL4A1 signal in IFE, placode, and hair germ stage. Each dot represents an individual fluorescence intensity measurement as shown in D. Larger dots show means of independent experiments. Error bars = SEM. ***P = <0.001, Mann–Whitney *U* test. ns = not significant. **(F)** Snapshots taken from a time-lapse live imaging movie of basal cell division in E15.5 *mTurq2-Col4a1/+;mTmG/mTmG* backskin. Interphase, metaphase, and post-cytokinesis stages are shown (left to right). The bottom panel shows the same images with membrane curvature measurements. Scale bar, 10 μm. **(G)** Quantification of the average angle of BM deformation as shown in F. Each dot represents an average of two angles. *n* = 23 dividing cells. Error bars = mean + SD. *P = <0.05 (0.0366), **P = <0.01, ***P = <0.001, one-way ANOVA with Dunn's multiple comparisons test. **(H)** Snapshots taken from time-lapse live imaging movies of placode, late-placode, and hair germ stages as labeled, in E14.5 and E15.5 *Col4a1/+;mTmG/mTmG* backskins. The bottom panel shows separate channels, note clear mTurq2-COL4A1 "baskets" surrounding the developing dermal condensate. Scale bar, 50 μm.

invaginating hair follicles, this suggests an inherent pliability of the epidermal BM during embryogenesis. BM stiffness has been shown to direct cellular behaviors and sculpt organs during development, and stiffer BMs are associated with cell migration and epithelial-to-mesenchymal transition (Crest et al., 2017; Ramos-Lewis and Page-McCaw, 2019; Wei et al., 2015). It is perhaps therefore intuitive that a BM underlying a rapidly proliferating progenitor cell layer during stratification needs to have sufficient pliability to allow cells to remain adhered throughout mitosis and to deform during morphogenesis.

Although we focused primarily on the epidermal BM for this study, PS Multiview imaging enabled visualization of a sharp delineation between the epidermis and dermis, with the dermis having a diffuse mTurq2-COL4A1 signal throughout, which was completely absent in the epidermis, consistent with dermal fibroblasts being the major source of collagen IV in the skin (Zorina et al., 2023; Video 1 and Fig. 5 H, bottom panels). Moreover, several other structures in the dermis showed robust mTurq2-COL4A1 localization, including vascular BMs and as yet unidentified migrating cells containing bright puncta of mTurq2-COL4A1 (Video 1 and Video 3). We also noticed a consistent diffuse mTurq2-COL4A1 signal in the dermis that coincided with the dermal condensate, underlying each hair follicle. Upon closer inspection, it appeared that a "basket" of collagen IV strands surrounds the cells of the dermal condensate as it develops (Fig. 5 H). This raises compelling questions regarding the role of collagen IV in maintaining the structural integrity of mesenchymal condensates during development, and it would be interesting to examine other mesenchymal condensates, such as those of the lung and kidney, to see if this phenomenon is conserved (Mammoto et al., 2011, 2015).

Fluorescence recovery after photobleaching (FRAP) shows collagen IVa1 in the epidermal BM is highly stable
Having established that our *mTurq2-Col4a1* mouse model is amenable to live imaging approaches, we next assayed the stability of mTurq2-COL4A1 in the epidermal BM of *mTurq2-Col4a1/+* backskins at E13.5 and E15.5, stages when the skin undergoes significant growth and morphological changes (stratification and hair follicle development). Several studies in invertebrates have shown that COL4A1 within the BM is highly immobile (Morrissey et al., 2016; Matsubayashi et al., 2017; Keeley et al., 2020). The half-life of BM proteins in the *Drosophila* embryo has been measured to be on the order of ∼7–10 h

(Matsubayashi et al., 2020). Additionally, a recent study in mice found that active secretion of vascular BM COL4A1 could only be detected early in development, suggesting that secretion thereafter, throughout adult life, may occur at much lower levels (Lartey et al., 2023). We therefore hypothesized that mTurq2-COL4A1 would be highly stable in the epidermal BM but may show increased mobility at E13.5 compared with E15.5 due to the rapid growth taking place during this earlier stage. We conducted FRAP on the interfollicular epidermal BM at both E13.5 and E15.5 and observed minimal mobility, with only a small mTurq2-COL4A1 mobile fraction of <15% at both stages (Fig. 6 C). We also performed FRAP on the BM around the rim of the hair follicle (E15.5), where the mTurq2-COL4A1 signal appears brightest (Fig. 6, A and B), and again observed minimal mTurq2-COL4A1 mobility. These data suggest that epidermal BM mTurq2-COL4A1 is highly stable within the epidermal BM, even as early as E13.5, consistent with other published datasets.

Discussion
Our understanding of the complexity of the BM has evolved significantly over the past few decades, and it is no longer considered a simple, static barrier between tissue compartments. Numerous studies have highlighted the critical roles that the BM plays in many physiological processes, including development, cell signaling, and disease progression (Töpfer, 2023; Pozzi et al., 2017; Randles et al., 2017; Banerjee et al., 2022). Elegant studies in *Drosophila* and *C. elegans* with fluorescently tagged BM components have significantly increased our understanding of the BM in terms of its interaction with neighboring cells and the mobility of individual components within it (Isabella and Horne-Badovinac, 2015; Keeley et al., 2020; Kelley et al., 2019; Clay and Sherwood, 2015; Van De Bor et al., 2021). However, until recently, the key bottleneck in our understanding of mammalian, and indeed vertebrate BMs, has been the lack of models in which endogenous BM components are labeled. Several attempts to generate such models have been unsuccessful (Shaw et al., 2020), and in vivo studies have relied upon knock-in reporters, which do not necessarily reflect endogenous protein expression and can be expressed ectopically and/or interfere with native protein function (Yamaguchi et al., 2022; Sztal et al., 2011; Futaki et al., 2023). The recent success by Morgner et al. (2023) in generating a *Lamb1-Dendra2* mouse model provided a proof-of-principle that fluorescently tagging
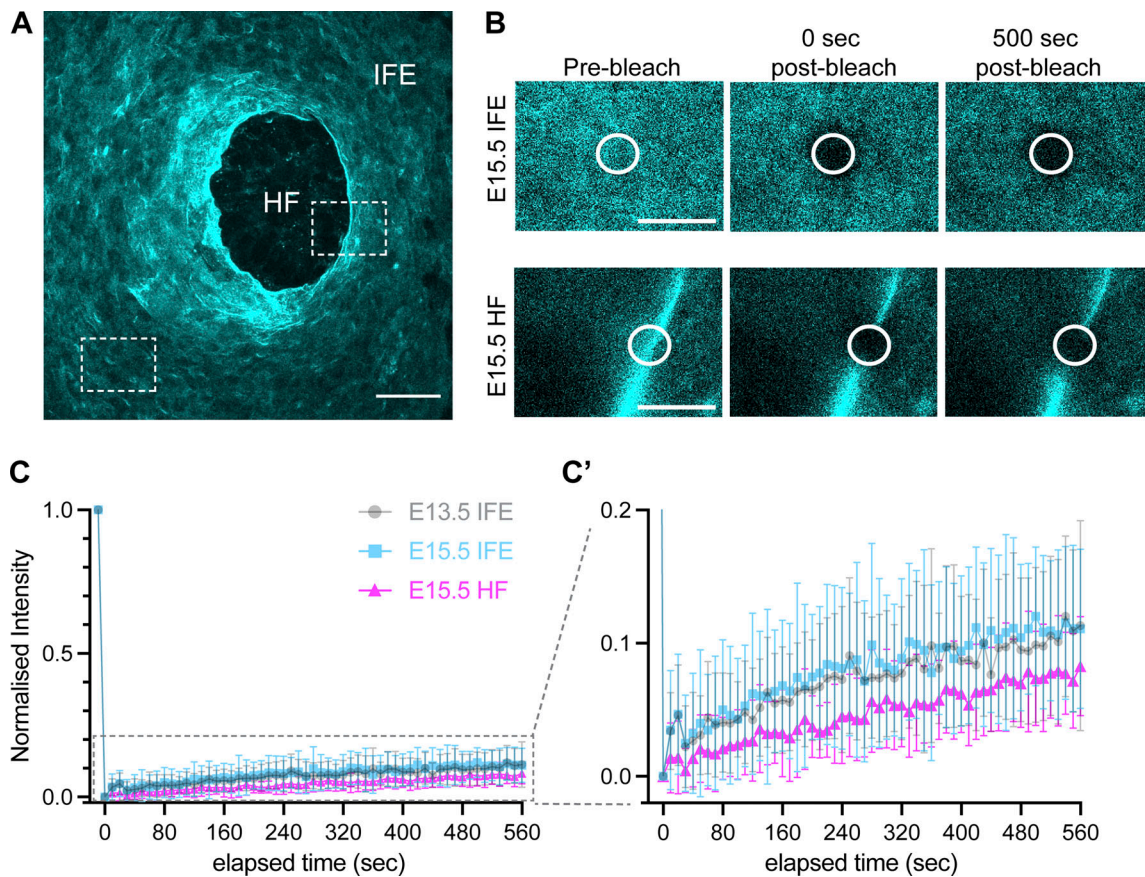
Figure 6. **mTurq2-COL4A1 is highly stable within the embryonic epidermal basement membrane. (A)** Planar overview of mTurq2-COL4A1 localization in E15.5 whole mount epidermis. White boxes indicate BM lying at the dermal–epidermal junction of the interfollicular epidermis (IFE) and along the rim of a budding hair follicle (HF). Scale bar, 25 µm. See also Video 3. **(B)** Still images from representative fluorescence recovery after photobleaching (FRAP) experiments of mTurq2-COL4A1 within the IFE (top panels) and rim of a hair follicle (bottom panels). Scale bars, 10 µm. **(C)** FRAP recovery curves of mTurq2-COL4A1 within the IFE at E13.5 (grey circles; $n = 36$), E15.5 (blue squares; $n = 32$), and at the rim of E15.5 hair follicles (magenta triangles; $n = 30$). Gray dotted box indicates the region rescaled in C'. Each point is the mean normalized intensity. Values were acquired across $n > 3$ biological replicates. Error bars = SD.

BM components in mice is feasible, and in this study, we have advanced one step further by generating a mouse line in which the BM ubiquitous COL4A1 is labeled. Collagen IV is the primary component of all BMs, and we, therefore, envisage that our *mTurq2-Col4a1* mouse will open up new possibilities to study many different aspects of BM biology, from developmental morphogenesis and wound healing to cancer metastasis. Moreover, several human diseases are linked specifically to mutations in collagen IV genes. Mutations in *COL4A1* and *COL4A2* have been linked to a wide range of human multisystem phenotypes, including ocular defects, porencephaly, cerebrovascular disease, and myopathy, collectively termed Gould's syndrome (Jeanne et al., 2012, 2015; Gould et al., 2005, 2006; Favor et al., 2007).

We focused on the epidermal BM for this study due to its accessibility and amenability to live imaging and because little is known about epidermal BM dynamics during embryonic development. Using the novel *mTurq2-Col4a1* mouse model combined with an innovative PS Multiview imaging approach, we have been able to long-term live-image the developing epidermal BM in embryonic mouse skin for the first time. Our findings reveal changes in epidermal BM morphology during hair follicle morphogenesis and suggest that the BM may be compressed by the forces generated by hair follicle invagination. We show that significant BM deformation also occurs during cell division, suggesting an inherent pliability of the epidermal BM during embryogenesis. Moreover, our observations that dividing basal progenitor cells remain adhered to the BM during mitosis challenge the existing assumption that all dividing cells significantly reduce their adhesions to the BM (Matus et al., 2014; Jones et al., 2019) and are in keeping with the integrin-rich contacts observed by Dix et al. (2018) during cell division. Our FRAP experiments provide a proof-of-principle that the *mTurq2-Col4a1* mouse line can be used to study and quantify COL4A1 mobility during assembly and our data agree with other studies demonstrating the highly stable nature of collagen IV within BMs, particularly the recent observations made by Lartey et al. (2023). The *Col4a1-P2A-eGFP* mouse line generated in their work labels cells that are actively secreting COL4A1 with eGFP. Because collagen IV is so stable, they wanted to determine when endothelial cells (EC) actively synthesize COL4A1 during development, as the presence of COL4A1 in vascular BMs does not necessarily mean it is being actively secreted. They showed that secretion of COL4A1 by EC occurs in a temporally restricted manner during development, with eGFP expression (and thus

Jones et al.
Live visualization of the murine basement membrane

Journal of Cell Biology 12 of 19
https://doi.org/10.1083/jcb.202309074

COL4A1 secretion) being detected during the period E8.5–E16.5 but not by E18.5, or in any of the adult organs they observed (including skin). Although it is possible that this observation reflects an inherent limitation of the mouse model, where subsequent COL4A1 secretion by EC is beyond the limits of detection, it is consistent with the idea that COL4A1, once established in a BM, is inherently very stable.

Importantly, although we focused on the epidermal BM in this study, the mTurq2-COL4A1 signal was observed in every physiological BM observed, in both embryos and adult tissues. Therefore, we foresee that there is a great deal to learn about mammalian BM morphology, remodeling, and mechanics that can be achieved using our *mTurq2-Col4a1* mouse.

A key limitation of this study is the homozygous lethality of the *mTurq2-Col4a1* mouse. Although we conducted several experiments to confirm that the BMs in *mTurq2-Col4a1/+* animals are indistinguishable from WT littermates, we have not been able to explain the lethality of the homozygous genotype. For studies of collagen IV protein biochemistry, therefore, the *mTurq2-Col4a1* mouse may not be the best suited model. One possible explanation for the absence of homozygous animals is that heterotrimers containing two mTurq2-COL4A1 molecules (collagen α1/α1/α2 [IV]) may cause problems with secretion; mutant COL4A1 or COL4A2 has been shown to accumulate within cells, reducing secretion and leading to extracellular deficiency (Jeanne et al., 2015). Inhibited secretion was also observed with C-terminal tagged human laminin β-1 in adenocarcinoma cells (Shaw et al., 2020). Alternatively, given that the 7S domain is important for crosslinking collagen IV into a lattice network, it may be that two mTurq2 molecules per collagen IV trimer interfere with 7S-mediated crosslinking, but one mTurq2 per trimer can be tolerated. Nevertheless, as the mTurq2-COL4A1 signal is bright and photostable in heterozygous *mTurq2-Col4a1/+* mice, this limitation does not impede the use of our mouse line to visualize BM dynamics live, in vivo. Furthermore, the *Lamb1-Dendra2* mouse, currently the only other mouse line in which a BM component is tagged at the endogenous level, is also largely homozygous lethal (Morgner et al., 2023). Finally, mTurquoise2 has an excitation/emission spectrum of 434/474 nm (Goedhart et al., 2012), necessitating the use of a 445-nm laser for optimal imaging results, which is often not included as part of the traditional laser confocal set-up. However, as the mTurquoise2 fluorescent protein is not excited by the 488 nm excitation wavelength for GFP, it can theoretically be used in combination with all three standard fluorescent protein combinations (i.e., GFP, mCherry/RFP, and far-red).

Using a novel *mTurq2-Col4a1* mouse model combined with an innovative PS Multiview imaging technique, we have visualized previously unobserved dynamics of developing skin. Our findings reveal unique insights into the epidermal BM during mouse embryonic development and highlight its inherent pliability in the context of morphological change. Although the large degree of growth, morphogenetic movement and cell division occurring during the period studied in this work suggested a need for the collagen IV supramolecular network to be extensively degraded, our observations show that once the collagen IV network is established early in development, it is not visibly diminished to accomodate morphogenesis, which may be due to either an equilibrium of degradation and secretion or an inherent pliability requiring little degradation to accommodate morphogenetic movements. Even during periods of rapid epithelial proliferation and morphogenetic change, mTurq2-COL4A1 within the epidermal BM is remarkably stable, showing minimal mobility. These data suggest that the observed pliability of the structure is a physical attribute of a relatively stable but flexible meshwork. Given the close association between increases in ECM stiffness, aging, cancer metastasis, and disease progression, our data raise questions about the behavioral changes cells might exhibit on a more rigid BM that can no longer yield to cellular forces. With the *mTurq2-Col4a1* mouse model in hand, these questions are now feasible to address.

Materials and methods

Generation and breeding of the *mTurq2-Col4a1* transgenic mouse line

The *mTurq2-Col4a1* mouse line was generated by knocking-in the coding sequence of *mTurquoise2* after the START codon and signal sequence of the endogenous *Col4a1* genomic locus to create an N-terminal fusion reporter using the previously described 2C-HR CRISPR method (Gu et al., 2020, 2018). Briefly, an HR repair plasmid was constructed by amplifying homology arms 1,000 bp upstream and downstream of the *mTurquoise2* insertion site by PCR from genomic DNA obtained from murine CD1 keratinocytes and inserted using InFusion cloning (Takara) into the *mTurquoise2-N1* plasmid (Addgene plasmid #54843; http://n2t.net/addgene:54843; RRID:Addgene_54843, a gift from Michael Davidson [Florida State University, Tallahassee, FL] and Dorus Gadella [University of Amsterdam, Netherlands]). Insertion was designed to remove the STOP codon at the 3′ end of the *mTurquoise2* ORF. Site-directed mutagenesis was then performed to silently mutate the PAM sites using NEB Q5 Site-Directed Mutagenesis kit (E0554) according to the manufacturer's instructions. sgRNAs were designed using CRISPOR (Concordet and Haeussler, 2018) and two were selected based on high predicted cutting efficiencies (sgRNA1 and sgRNA2). Synthetic sgRNAs were then ordered from Synthego with chemical modifications at the 5′ and 3′ termini: 2′-O-methyl modified bases and 3′ phosphorothioate linkages; for sequences see Table S1; sgRNAs were provided in donor vectors by Synthego. CD1-IGS mice (Charles River strain 022) were used as embryo donors. Briefly, female CD1-IGS were super-ovulated at 5–7 wk of age using 7.5 IU PMSG (Biovendor) administered by IP injection followed by 7.5 IU HCG (Sigma-Aldrich) by IP injection 47 h post PMSG. Superovulated females were mated to CD1-IGS stud males and checked for copulatory plugs the following morning. Cytoplasmic microinjection of two-cell embryos was performed as previously described (Gu et al., 2020, 2018). Briefly, embryos were harvested at the two-cell stage at E1.5 by flushing the oviducts with M2 Media (Cytospring), and each cell was microinjected with 100 ng/μl *Cas9* mRNA (made by in vitro transcription [mMESSAGE mMACHINE SP6 transcription kit; Thermo Fisher Scientific] using Addgene plasmid 122948), 30 ng/μl donor plasmid, and 50 ng/μl sgRNA using a Leica Dmi8

Jones et al.
Live visualization of the murine basement membrane

Journal of Cell Biology   13 of 19
https://doi.org/10.1083/jcb.202309074

inverted epifluorescent microscope, an Eppendorf Femtojet, and a Micro-ePore (WPI). Embryos were immediately transferred into the oviducts of pseudo-pregnant female CD1 mice. CD1 mice were used to generate the line as they tend to produce larger litter sizes than the C57BL/6J, thus increasing the probability of identifying a founder. Positive founders (N0) were identified by PCR genotyping as follows. gDNA from pup ear punches was prepared using Purelink Genomic DNA Mini Kit (Invitrogen) before being used as the template in two PCR reactions. Genotyping PCRs were designed to (i) only amplify a fragment if insertion had occurred at the correct locus and (ii) differentiate between hetero- and homozygotes by spanning the entire insertion area. See Table S1 for primer sequences. N0 founders were then crossed to C57BL/6J mice, and N1 mice from these crosses were genotyped as above using a proofreading polymerase (Q5 DNA Polymerase; NEB). Purified amplicons from these PCR reactions were then Sanger sequenced to ensure the accuracy of the insertion site and fidelity of the genomic sequence. N1 mTurq2-Col4a1 heterozygotes were then outcrossed to C57BL/6J mice for a minimum of five generations. Heterozygote incrosses from all generations did not yield any homozygous offspring, and litters were slightly smaller as a result but were otherwise Mendelian in ratio. All experiments were conducted in biological triplicate as a minimum, with technical replicates where appropriate. Embryos were obtained from pregnant dams at E11.5–E15.5 and all embryos of the correct genotype were used, without consideration of sex. Mice were housed in an AAALAC-accredited facility following the Guide for the Care and Use of Laboratory Animals. Animal maintenance and husbandry followed the Laboratory Animal Welfare Act. Princeton University's Institutional Animal Care and Use Committee (IACUC) approved all animal procedures, and the three "R"s were considered in all experimental design.

Immunofluorescence and fixed sample imaging

The following mouse tissues were embedded fresh in OCT on dry ice and stored at –80°C: E18.5 embryos, dissected in PBS and heads removed; adult kidneys, whole; adult back skin, shaved using clippers to remove the hair and dissected into strips along the midline. Frozen OCT-embedded tissues were cryosectioned on a Leica CM3050 cryostat. Sagittal sections were cut at 10 μm thickness, collected on Superfrost Plus slides, and allowed to dry before being stored at –20°C. For immunostaining, sections were moved to a slide holder container and fixed in 4% paraformaldehyde (PFA) in PBS for 10 min at room temperature (RT), washed in PBS for 5 min, permeabilized in PBT2 (PBS with 0.2% Triton X-100) for 10 min at RT, and blocked in 2% normal goat serum, 2% normal donkey serum, and 2% bovine serum albumin (BSA) in PBT2 overnight at 4°C with gentle rocking. Slides were moved to a humidified chamber on a flat surface and incubated with a primary antibody in blocking medium for 1 h at RT; see Table S2 for primary antibodies and concentrations used. Slides were washed in slide holder containers three times for 10 min with PBT2 and incubated in a humidified chamber on a flat surface with secondary antibodies in PBT2 for 1 h at RT. Alexa Fluor-555 and -647 secondary antibodies were used at 1:2,000 (Invitrogen). Slides were washed in slide holder

containers in PBT2 with Hoechst (1 μg/ml, H1399; Invitrogen) for 10 min, followed by two 10 min washes in PBT2. A final wash in PBS for 5 min was carried out before mounting in ProLong Gold (P36930; Invitrogen). Slides were stored at –20°C until imaged.

For immunofluorescence of E16.5, E15.5, and E12.5 backskins, embryos were dissected in PBS (+Mg, +Ca) and fixed in 4% PFA for 1 h (1.5 h for E16.5) at RT with gentle rocking. Backskins were then incubated in blocking medium overnight at 4°C with gentle rocking (1% BSA, 1% fish gelatin, 2% normal goat serum, and 2% normal donkey serum in PBT2 with 0.01% sodium azide). The following day, samples were incubated in primary antibody (in blocking medium) overnight at 4°C with gentle rocking. See Table S2 for primary antibody details and concentrations used. Samples were then washed a minimum of five times (30 min per wash) in PBT2 before incubating overnight in secondary antibodies (Alexa Fluor-555 and -647, 1:1,000; Invitrogen) in PBT2 at 4°C with gentle rocking in the dark. Following secondary incubation, samples were washed a minimum of five times in PBT2 (30 min per wash), with the first wash containing Hoechst (H1399, 1 μg/ml; Invitrogen), before being mounted in ProLong Gold (P36930; Invitrogen).

Images of E15.5 and E12.5 backskins were acquired on an inverted Nikon A1R confocal microscope controlled by NIS Elements software. Objectives used were Plan Apo 10/0.45NA air, Plan Apo 20/0.75NA air, and Plan Apo 60/1.4NA oil immersion (Nikon). For XZ optical reconstructions, resonance imaging was used with 8× averaging and images denoised in NIS Elements. NIS Elements and FIJI were used for all image processing. Images of E16.5 backskins were acquired on a Nikon inverted CSU-W1 SoRa Spinning Disk microscope with a Plan Apo 60× Oil/1.4NA immersion objective, controlled by NIS Elements software. Images were processed using NIS Elements and FIJI.

Pearson's correlation coefficient and overlap fraction analyses

Images were acquired as described above using a Plan Apo 60/1.4NA oil immersion objective with 6× zoom to obtain a pixel size of 0.09 μm and an optical resolution of 0.26 μm (to attain Nyquist). Z stacks were obtained with 0.3 μm step size over a range of 3 μm with the center of the stack being set at the epidermal BM. 10 individual Z-stacks were obtained per embryo ($n = 3$). To calculate Pearson's Correlation Coefficient, the Z slice at which the epidermal BM was most in focus was selected, background-subtracted, and the FIJI plugin Coloc 2 (Costes threshold regression; Costes randomizations = 100) was used on a region of interest (ROI) around the area of laminin β-1 signal (avoiding areas devoid of signal to reduce noise). Both biological ($n = 3$) and technical ($n = 30$) replicates were plotted and statistical analysis was undertaken using GraphPad Prism.

Overlap fraction analysis was undertaken using a custom macro in FIJI. Single Z planes in both channels as described above were thresholded using the Otsu method to generate a mask. The overlap map was then thresholded (Otsu) and an ROI was generated around the entire overlap region. The area of the overlap region was then divided by the area of the mask for each channel to calculate the overlap fraction. Both biological ($n = 3$) and technical ($n = 30$) replicates were plotted and statistical analysis was undertaken using GraphPad Prism.

Transmission electron microscopy (TEM)

E18.5 embryos were harvested from the euthanized dam and backskins were immediately dissected into fresh TEM fixative (2% glutaraldehyde, 4% formaldehyde, 2 mM $CaCl_2$ in 0.1 M sodium cacodylate buffer, pH 7.2). Samples were gently rocked at RT for 1 h before storage at 4°C until processed for imaging. Samples were postfixed in 1% osmium tetroxide and processed for Epon embedding. Ultrathin sections (60–65 nm) were counterstained with uranyl acetate and lead citrate. Images were taken with a transmission electron microscope (Tecnai G2-12; FEI) equipped with a digital camera (AMT BioSprint29).

PS Multiview live imaging

A stencil to create a ridge in the agarose gel was created using Conair bobby pins and a standard glass microscope slide (Fisherbrand). Three bobby pins were cut at the apex, and then the flat arms from each pin were super glued side-on to a microscope slide. This created a flat surface with a large bar in the center measuring 3 mm wide, 25 mm long, and 1 mm tall. F-medium agarose plates were then made as previously described (Cetera et al., 2018) with the following additional steps. After briefly cooling to 60°C, the liquid agarose medium was poured into a 35-mm dish plate at 4°C. After 2 min had elapsed, the bobby pin glass stencil was dropped onto the solidifying gel, allowing it to float on top. After 15 min at RT, the bobby pin glass stencil was carefully removed from the gel using forceps. The ridged gel was then stored in a 37°C, 5% CO_2 cell-culture incubator while dissections took place. E14.5 and E15.5 flank skin explants were dissected in PBS (+Mg, +Ca), as previously described (Cetera et al., 2018), and transferred to the agarose-F-medium gel with the ridge. The explants were mounted dermal side down with ~50% of the lateral flank region being placed over the edge of the ridge and the midline region was mounted firmly on the flat portion of the gel to prevent slipping into the ridge. Explant gels were then mounted into Lumox membrane dishes (Sarstedt) as previously described. Z-stacks with 3-μm step sizes were then acquired over several XY positions at 7-min intervals for 5–15 h using a Nikon inverted CSU-W1 SoRa Spinning Disk microscope with a Plan Apo Lambda S 40XC Sil/1.25NA immersion objective, controlled by NIS Elements software. Sample temperature was maintained during imaging using a Tokai Hit humidified stage top incubator and an environmental imaging chamber, both set to 37°C with 5% CO_2. Throughout all imaging experiments, areas that were close to the edge of the explants were not imaged to avoid any wound-healing response. NIS Elements and FIJI were used for movie processing.

Live-image analysis and quantification

The mTurq2-COL4A1 signal intensity was determined during PS Multiview imaging using FIJI software. An ROI was drawn both around the mTurq2-COL4A1 signal at the base of the hair follicle and around the interfollicular epidermis (IFE) region in view. If the hair follicle was in the center of the image, two IFE ROIs were drawn on either side of the hair follicle, and then the mean values were obtained. The average intensity of the mTurq2-COL4A1 signal in both hair follicle and IFE ROIs was then measured, and the ratio between the two was then calculated for

each time point across the different movies (n = 8 movies). The two stages of hair follicle development (placode and hair germ) were determined by measuring the depth of the hair follicle relative to the IFE at every time point across all movies and then binning the different depths into two equal groups, representing the two developmental stages. The background IFE/IFE ratio was determined by taking each individual IFE mTurq2-COL4A1 signal intensity measurement and dividing it by the average IFE mTurq2-COL4A1 signal for the corresponding movie. Graphing and statistical analysis were undertaken using GraphPad Prism.

To measure BM deformation occurring during cell division, we identified dividing basal progenitor cells and measured the angle between the dividing cell's most basal contact with that of both of its closest neighbors. The center of the basal surface of the dividing cell and the two neighboring cells, together with the basal most intersection of the two neighboring cells, were used as the points from which to measure the angles. The angles were measured at three timepoints: 18 min before the onset of division when the cell is in interphase (columnar), during metaphase when the cell rounds up, and 18 min after the daughter cells separate. The mean of both angles at each time point was calculated and plotted, n = 23 dividing cells that were followed through division. Graphing and statistical analysis were undertaken using GraphPad Prism.

FRAP

BMs in live skin explants from E13.5 or E15.5 *mTurq2-Col4a1/+* embryos were imaged using a Plan Apo 20/0.45NA air objective (Nikon) with appropriate optical zoom on an inverted Nikon A1R laser scanning confocal microscope equipped with a stage-top Tokai Hit incubation chamber to maintain 37°C and 5% CO_2. 1.5 μm diameter circular ROIs were bleached using a 445-nm laser, and recovery was monitored for a period of 10 min with 10-s intervals from either IFE or along the rim of developing hair follicles. Three reference prebleach images were also acquired. Magnification, laser power (both for bleach and acquisition), pixel dwell time, and acquisition rate were kept uniform across all measurements. The acquired images and measured ROIs in the time series were checked for Z-drift and corrected for the presence of any XY drift. A reference ROI was made in a non-bleached region to correct for overall bleaching during image acquisition. Background autofluorescence was measured from non-fluorescent WT skin using the same image acquisition conditions. The ROI values were extracted from drift-corrected images in NIS Elements software and subsequently processed in Microsoft Excel and GraphPad Prism. Each image time series was background/autofluorescence subtracted and bleach corrected (to be referred to as corrected intensity henceforth) and thereafter the corrected intensity profile was normalized as (F_t – F_{bleach})/ (F_{ini} – F_{bleach}), where F_t is the corrected intensity of the ROI at a given time point, F_{bleach} is the corrected intensity at the time point immediately after bleaching, and F_{ini} is the mean ROI intensity of the three pre-bleach frames. Each mean recovery curve was fitted to an exponential one-phase association equation in GraphPad Prism with an r-squared value >0.9 to determine the fitted plateau and Y_0 values, which were then used to determine the immobile fraction = 1- [(Plateau-Y_0)/(1- Y_0)]. Data represented are pooled from three biological replicates.

Online supplemental material

Fig. S1, related to Fig. 1, shows an additional experimental replicate of mTurq2-COL4A1 labeling in adult mouse skin and kidney. Fig. S2, related to Fig. 3, shows TEM images from additional experimental replicates of E18.5 WT and *mTurq2-Col4a1/+* embryonic skin. Fig. S3, related to Fig. 5, shows additional examples of snapshots taken from time-lapse imaging of BM curvature around dividing basal progenitor cells in *mTurq2-Col4a1/+;mTmG/mTmG* backskins, and quantification of the average angle of deformation and maintained hemidesmosome adhesions in dividing cells by integrin β4 antibody labeling and TEM. Video 1 shows three representative time-lapse live-imaging movies of hair follicle invagination in E14.5-E15.5 *mTurq2-Col4a1/+;mTmG/mTmG* backskins. Video 2 shows three representative time-lapse live-imaging movies of basal progenitor cell divisions in E14.5–E15.5 *mTurq2-Col4a1/+;mTmG/mTmG* backskins. Video 3 shows a Z-stack movie in planar view through a fixed E15.5 *mTurq2-Col4a1/+* backskin from the basal layer (basement membrane) through to the dermis. Table S1 details sgRNA and oligonucleotide sequences used in this study; Table S2 details the primary antibodies used.

References

Akhmanova, M., S. Emtenani, D. Krueger, A. Gyoergy, M. Guarda, M. Vlasov, F. Vlasov, A. Akopian, A. Ratheesh, S. De Renzis, and D.E. Siekhaus. 2022. Cell division in tissues enables macrophage infiltration. *Science*. 376:394–396. https://doi.org/10.1126/science.abj0425

Albini, A., and D.M. Noonan. 2010. The 'chemoinvasion' assay, 25 years and still going strong: The use of reconstituted basement membranes to study cell invasion and angiogenesis. *Curr. Opin. Cell Biol.* 22:677–689. https://doi.org/10.1016/j.ceb.2010.08.017

Bahr, J.C., X.-Y. Li, T.Y. Feinberg, L. Jiang, and S.J. Weiss. 2022. Divergent regulation of basement membrane trafficking by human macrophages and cancer cells. *Nat. Commun.* 13:6409. https://doi.org/10.1038/s41467-022-34087-x

Banerjee, S., J. Isaacman-Beck, V.A. Schneider, and M. Granato. 2013. A novel role for Lh3 dependent ECM modifications during neural crest cell migration in zebrafish. *PLoS One.* 8:e54609. https://doi.org/10.1371/journal.pone.0054609

Banerjee, S., W.-C. Lo, P. Majumder, D. Roy, M. Ghorai, N.K. Shaikh, N. Kant, M.S. Shekhawat, V.S. Gadekar, S. Ghosh, et al. 2022. Multiple roles for basement membrane proteins in cancer progression and EMT. *Eur. J. Cell Biol.* 101:151220. https://doi.org/10.1016/j.ejcb.2022.151220

Behrens, D.T., D. Villone, M. Koch, G. Brunner, L. Sorokin, H. Robenek, L. Bruckner-Tuderman, P. Bruckner, and U. Hansen. 2012. The epidermal basement membrane is a composite of separate laminin- or collagen IV-containing networks connected by aggregated perlecan, but not by nidogens. *J. Biol. Chem.* 287:18700–18709. https://doi.org/10.1074/jbc.M111.336073

Box, K., B.W. Joyce, and D. Devenport. 2019. Epithelial geometry regulates spindle orientation and progenitor fate during formation of the mammalian epidermis. *Elife.* 8:e47102. https://doi.org/10.7554/eLife.47102

Buszczak, M., S. Paterno, D. Lighthouse, J. Bachman, J. Planck, S. Owen, A.D. Skora, T.G. Nystul, B. Ohlstein, A. Allen, et al. 2007. The carnegie protein trap library: A versatile tool for Drosophila developmental studies. *Genetics.* 175:1505–1531. https://doi.org/10.1534/genetics.106.065961

Cetera, M., L. Leybova, B. Joyce, and D. Devenport. 2018. Counter-rotational cell flows drive morphological and cell fate asymmetries in mammalian hair follicles. *Nat. Cell Biol.* 20:541–552. https://doi.org/10.1038/s41556-018-0082-7

Champion, L., M.I. Linder, and U. Kutay. 2017. Cellular reorganization during mitotic entry. *Trends Cell Biol.* 27:26–41. https://doi.org/10.1016/j.tcb.2016.07.004

Chan, A., and T. Mauro. 2011. Acidification in the epidermis and the role of secretory phospholipases. *Dermatoendocrinol.* 3:84–90. https://doi.org/10.4161/derm.3.2.15140

Chlasta, J., P. Milani, G. Runel, J.-L. Duteyrat, L. Arias, L.-A. Lamiré, A. Boudaoud, and M. Grammont. 2017. Variations in basement membrane mechanics are linked to epithelial morphogenesis. *Development.* 144:4350–4362. https://doi.org/10.1242/dev.152652

Clay, M.R., and D.R. Sherwood. 2015. Basement membranes in the worm: A dynamic scaffolding that instructs cellular behaviors and shapes tissues. *Curr. Top. Membr.* 76:337–371. https://doi.org/10.1016/bs.ctm.2015.08.001

Concordet, J.-P., and M. Haeussler. 2018. CRISPOR: Intuitive guide selection for CRISPR/Cas9 genome editing experiments and screens. *Nucleic Acids Res.* 46:W242-W245. https://doi.org/10.1093/nar/gky354

Costa, D.S., I.W. Kenny-Ganzert, Q. Chi, K. Park, L.C. Kelley, A. Garde, D.Q. Matus, J. Park, S. Yogev, B. Goldstein, et al. 2023. The Caenorhabditis elegans anchor cell transcriptome: Ribosome biogenesis drives cell invasion through basement membrane. *Development.* 150:dev201570. https://doi.org/10.1242/dev.201570

Costantini, L.M., M. Fossati, M. Francolini, and E.L. Snapp. 2012. Assessing the tendency of fluorescent proteins to oligomerize under physiologic conditions. *Traffic.* 13:643–649. https://doi.org/10.1111/j.1600-0854.2012.01336.x

Crest, J., A. Diz-Muñoz, D.-Y. Chen, D.A. Fletcher, and D. Bilder. 2017. Organ sculpting by patterned extracellular matrix stiffness. *Elife.* 6:e24958. https://doi.org/10.7554/eLife.24958

Damen, M., L. Wirtz, E. Soroka, H. Khatif, C. Kukat, B.D. Simons, and H. Bazzi. 2021. High proliferation and delamination during skin epidermal stratification. *Nat. Commun.* 12:3227. https://doi.org/10.1038/s41467-021-23386-4

Denda, M., J. Hosoi, and Y. Asida. 2000. Visual imaging of ion distribution in human epidermis. *Biochem. Biophys. Res. Commun.* 272:134–137. https://doi.org/10.1006/bbrc.2000.2739

Dix, C.L., Matthews, H.K., Uroz, M., Mclaren, S., Wolf, L., Heatley, N., Win, Z., Almada, P., Henriques, R. & Boutros, M. 2018. The role of mitotic cell-substrate adhesion re-modeling in animal cell division. *Dev. Cell*. 45: 132–145. e3. https://doi.org/10.1016/j.devcel.2018.03.009

Favor, J., C.J. Gloeckner, D. Janik, M. Klempt, A. Neuhäuser-Klaus, W. Pretsch, W. Schmahl, and L. Quintanilla-Fend. 2007. Type IV procollagen missense mutations associated with defects of the eye, vascular stability, the brain, kidney function and embryonic or postnatal viability in the mouse, Mus musculus: An extension of the Col4a1 allelic series and the identification of the first two Col4a2 mutant alleles. *Genetics*. 175: 725–736. https://doi.org/10.1534/genetics.106.064733

Frantz, C., K.M. Stewart, and V.M. Weaver. 2010. The extracellular matrix at a glance. *J. Cell Sci*. 123:4195–4200. https://doi.org/10.1242/jcs.023820

Futaki, S., A. Horimoto, C. Shimono, N. Norioka, Y. Taniguchi, H. Hamaoka, M. Kaneko, M. Shigeta, T. Abe, K. Sekiguchi, and Y. Kondo. 2023. Visualization of basement membranes by a nidogen-based fluorescent reporter in mice. *Matrix Biol. Plus*. 18:100133. https://doi.org/10.1016/j.mbplus.2023.100133

Glentis, A., P. Oertle, P. Mariani, A. Chikina, F. El Marjou, Y. Attieh, F. Zaccarini, M. Lae, D. Loew, F. Dingli, et al. 2017. Cancer-associated fibroblasts induce metalloprotease-independent cancer cell invasion of the basement membrane. *Nat. Commun*. 8:924. https://doi.org/10.1038/s41467-017-00985-8

Goedhart, J., D. von Stetten, M. Noirclerc-Savoye, M. Lelimousin, L. Joosen, M.A. Hink, L. van Weeren, T.W.J. Gadella Jr, and A. Royant. 2012. Structure-guided evolution of cyan fluorescent proteins towards a quantum yield of 93%. *Nat. Commun*. 3:751. https://doi.org/10.1038/ncomms1738

Gould, D.B., F.C. Phalan, G.J. Breedveld, S.E. van Mil, R.S. Smith, J.C. Schimenti, U. Aguglia, M.S. van der Knaap, P. Heutink, and S.W. John. 2005. Mutations in Col4a1 cause perinatal cerebral hemorrhage and porencephaly. *Science*. 308:1167–1171. https://doi.org/10.1126/science.1109418

Gould, D.B., F.C. Phalan, S.E. van Mil, J.P. Sundberg, K. Vahedi, P. Massin, M.G. Bousser, P. Heutink, J.H. Miner, E. Tournier-Lasserve, and S.W. John. 2006. Role of COL4A1 in small-vessel disease and hemorrhagic stroke. *N. Engl. J. Med*. 354:1489–1496. https://doi.org/10.1056/NEJMoa053727

Gu, B., E. Posfai, and J. Rossant. 2018. Efficient generation of targeted large insertions by microinjection into two-cell-stage mouse embryos. *Nat. Biotechnol*. 36:632–637. https://doi.org/10.1038/nbt.4166

Gu, B., E. Posfai, M. Gertsenstein, and J. Rossant. 2020. Efficient generation of large-fragment knock-in mouse models using 2-cell (2C)-homologous recombination (HR)-CRISPR. *Curr. Protoc. Mouse Biol*. 10:e67. https://doi.org/10.1002/cpmo.67

Gunwar, S., F. Ballester, M.E. Noelken, Y. Sado, Y. Ninomiya, and B.G. Hudson. 1998. Glomerular basement membrane. Identification of a novel disulfide-cross-linked network of α3, α4, and α5 chains of type IV collagen and its implications for the pathogenesis of Alport syndrome. *J. Biol. Chem*. 273:8767–8775. https://doi.org/10.1074/jbc.273.15.8767

Guo, X.D., and J.M. Kramer. 1989. The two Caenorhabditis elegans basement membrane (type IV) collagen genes are located on separate chromosomes. *J. Biol. Chem*. 264:17574–17582. https://doi.org/10.1016/S0021-9258(18)71530-5

Guo, X.D., J.J. Johnson, and J.M. Kramer. 1991. Embryonic lethality caused by mutations in basement membrane collagen of C. elegans. *Nature*. 349: 707–709. https://doi.org/10.1038/349707a0

Harmansa, S., A. Erlich, C. Eloy, G. Zurlo, and T. Lecuit. 2023. Growth anisotropy of the extracellular matrix shapes a developing organ. *Nat. Commun*. 14:1220. https://doi.org/10.1038/s41467-023-36739-y

Harunaga, J.S., A.D. Doyle, and K.M. Yamada. 2014. Local and global dynamics of the basement membrane during branching morphogenesis require protease activity and actomyosin contractility. *Dev. Biol*. 394:197–205. https://doi.org/10.1016/j.ydbio.2014.08.014

Hohenester, E., and P.D. Yurchenco. 2013. Laminins in basement membrane assembly. *Cell Adh. Migr*. 7:56–63. https://doi.org/10.4161/cam.21831

Huszka, G., and M.A. Gijs. 2019. Super-resolution optical imaging: A comparison. *Micro Nano Eng*. 2:7–28. https://doi.org/10.1016/j.mne.2018.11.005

Hynes, R.O. 1992. Integrins: Versatility, modulation, and signaling in cell adhesion. *Cell*. 69:11–25. https://doi.org/10.1016/0092-8674(92)90115-S

Isabella, A.J., and S. Horne-Badovinac. 2015. Dynamic regulation of basement membrane protein levels promotes egg chamber elongation in Drosophila. *Dev. Biol*. 406:212–221. https://doi.org/10.1016/j.ydbio.2015.08.018

Jeanne, M., C. Labelle-Dumais, J. Jorgensen, W.B. Kauffman, G.M. Mancini, J. Favor, V. Valant, S.M. Greenberg, J. Rosand, and D.B. Gould. 2012.

COL4A2 mutations impair COL4A1 and COL4A2 secretion and cause hemorrhagic stroke. *Am. J. Hum. Genet*. 90:91–101. https://doi.org/10.1016/j.ajhg.2011.11.022

Jeanne, M., J. Jorgensen, and D.B. Gould. 2015. Molecular and genetic analyses of collagen type IV mutant mouse models of spontaneous intracerebral hemorrhage identify mechanisms for stroke prevention. *Circulation*. 131:1555–1565. https://doi.org/10.1161/CIRCULATIONAHA.114.013395

Jones, F.E., M.A. Bailey, L.S. Murray, Y. Lu, S. McNeilly, U. Schlötzer-Schrehardt, R. Lennon, Y. Sado, D.G. Brownstein, J.J. Mullins, et al. 2016. ER stress and basement membrane defects combine to cause glomerular and tubular renal disease resulting from Col4a1 mutations in mice. *Dis. Model. Mech*. 9:165–176. https://doi.org/10.1242/dmm.021741

Jones, M.C., J. Zha, and M.J. Humphries. 2019. Connections between the cell cycle, cell adhesion and the cytoskeleton. *Philos. Trans. R. Soc. Lond. B Biol. Sci*. 374:20180227. https://doi.org/10.1098/rstb.2018.0227

Keeley, D.P., E. Hastie, R. Jayadev, L.C. Kelley, Q. Chi, S.G. Payne, J.L. Jeger, B.D. Hoffman, and D.R. Sherwood. 2020. Comprehensive endogenous tagging of basement membrane components reveals dynamic movement within the matrix scaffolding. *Dev. Cell*. 54:60–74.e7. https://doi.org/10.1016/j.devcel.2020.05.022

Keene, D.R., and S.F. Tufa. 2020. Connective tissue ultrastructure: A direct comparison between conventional specimen preparation and high-pressure freezing/freeze-substitution. *Anat. Rec*. 303:1514–1526. https://doi.org/10.1002/ar.24211

Kelley, L.C., L.L. Lohmer, E.J. Hagedorn, and D.R. Sherwood. 2014. Traversing the basement membrane in vivo: A diversity of strategies. *J. Cell Biol*. 204:291–302. https://doi.org/10.1083/jcb.201311112

Kelley, L.C., Wang, Z., Hagedorn, E.J., Wang, L., Shen, W., Lei, S., Johnson, S.A. & Sherwood, D.R. 2017. Live-cell confocal microscopy and quantitative 4D image analysis of anchor-cell invasion through the basement membrane in Caenorhabditis elegans. *Nat. protoco*. 12:2081–2096. https://doi.org/10.1038/nprot.2017.093

Kelley, L.C., Q. Chi, R. Cáceres, E. Hastie, A.J. Schindler, Y. Jiang, D.Q. Matus, J. Plastino, and D.R. Sherwood. 2019. Adaptive F-actin polymerization and localized ATP production drive basement membrane invasion in the absence of MMPs. *Dev. Cell*. 48:313–328.e8. https://doi.org/10.1016/j.devcel.2018.12.018

Kenny-Ganzert, I.W., and D.R. Sherwood. 2024. The C. elegans anchor cell: A model to elucidate mechanisms underlying invasion through basement membrane. *Semin. Cell Dev. Biol*. 154:23–34. https://doi.org/10.1016/j.semcdb.2023.07.002

Komori, T., M. Ono, E.S. Hara, J. Ueda, H.T.T. Nguyen, H.T. Nguyen, T. Yonezawa, T. Maeba, A. Kimura-Ono, T. Takarada, et al. 2018. Type IV collagen α6 chain is a regulator of keratin 10 in keratinization of oral mucosal epithelium. *Sci. Rep*. 8:2612. https://doi.org/10.1038/s41598-018-21000-0

Kruegel, J., and N. Miosge. 2010. Basement membrane components are key players in specialized extracellular matrices. *Cell. Mol. Life Sci*. 67: 2879–2895. https://doi.org/10.1007/s00018-010-0367-x

Lambert, T.J. 2019. FPbase: A community-editable fluorescent protein database. *Nat. Methods*. 16:277–278. https://doi.org/10.1038/s41592-019-0352-8

Lartey, N.L., M. van der Ent, R. Alonzo, D. Chen, and P.D. King. 2023. A temporally-restricted pattern of endothelial cell collagen 4 alpha 1 expression during embryonic development determined with a novel knockin Col4a1-P2A-eGFP mouse line. *Genesis*. 27:e23539. https://doi.org/10.1002/dvg.23539

LeBleu, V.S., B. Macdonald, and R. Kalluri. 2007. Structure and function of basement membranes. *Exp. Biol. Med*. 232:1121–1129. https://doi.org/10.3181/0703-MR-72

Leonard, C.E., and L.A. Taneyhill. 2020. The road best traveled: Neural crest migration upon the extracellular matrix. *Semin. Cell Dev. Biol*. 100: 177–185. https://doi.org/10.1016/j.semcdb.2019.10.013

Lock, J.G., M.C. Jones, J.A. Askari, X. Gong, A. Oddone, H. Olofsson, S. Göransson, M. Lakadamyali, M.J. Humphries, and S. Strömblad. 2018. Reticular adhesions are a distinct class of cell-matrix adhesions that mediate attachment during mitosis. *Nat. Cell Biol*. 20:1290–1302. https://doi.org/10.1038/s41556-018-0220-2

Ma, M., Cao, X., Dai, J. and Pastor-Pareja, J.C. 2017. Basement membrane manipulation in Drosophila wing discs affects Dpp retention but not growth mechanoregulation. *Dev. Cell*. 42:97–106. e4. https://doi.org/10.1016/j.devcel.2017.06.004

Mak, K.M., and R. Mei. 2017. Basement membrane type IV collagen and laminin: An overview of their biology and value as fibrosis biomarkers

of liver disease. *Anat. Rec.* 300:1371–1390. https://doi.org/10.1002/ar.23567

Mammoto, T., A. Mammoto, Y.-S. Torisawa, T. Tat, A. Gibbs, R. Derda, R. Mannix, M. de Bruijn, C.W. Yung, D. Huh, and D.E. Ingber. 2011. Mechanochemical control of mesenchymal condensation and embryonic tooth organ formation. *Dev. Cell.* 21:758–769. https://doi.org/10.1016/j.devcel.2011.07.006

Mammoto, T., A. Mammoto, A. Jiang, E. Jiang, B. Hashmi, and D.E. Ingber. 2015. Mesenchymal condensation-dependent accumulation of collagen VI stabilizes organ-specific cell fates during embryonic tooth formation. *Dev. Dyn.* 244:713–723. https://doi.org/10.1002/dvdy.24264

Matsubayashi, Y., A. Louani, A. Dragu, B.J. Sánchez-Sánchez, E. Serna-Morales, L. Yolland, A. Gyoergy, G. Vizcay, R.A. Fleck, J.M. Heddleston, et al. 2017. A moving source of matrix components is essential for De novo basement membrane formation. *Curr. Biol.* 27:3526–3534.e4. https://doi.org/10.1016/j.cub.2017.10.001

Matsubayashi, Y., B.J. Sanchez-Sanchez, S. Marcotti, E. Serna-Morales, A. Dragu, G. Vizcay-Barrena, R.A. Fleck, and B.M.Stramer. 2020. Rapid homeostatic turnover of embryonic ECM during tissue morphogenesis. *Dev. Cell.* 54:33–42.e9. https://doi.org/10.1016/j.devcel.2020.06.005

Matus, D.Q., E. Chang, S.C. Makohon-Moore, M.A. Hagedorn, Q. Chi, and D.R. Sherwood. 2014. Cell division and targeted cell cycle arrest opens and stabilizes basement membrane gaps. *Nat. Commun.* 5:4184. https://doi.org/10.1038/ncomms5184

McGrath, J.A., A. Ishida-Yamamoto, H. Shimizu, J.D. Fine, and R.A. Eady. 1994. Immunoelectron microscopy of skin basement membrane zone antigens: A pre-embedding method using 1-nm immunogold with silver enhancement. *Acta Derm. Venereol.* 74:197–200. https://doi.org/10.2340/0001555574201205

Micalizzi, D.S., S.M. Farabaugh, and H.L. Ford. 2010. Epithelial-mesenchymal transition in cancer: Parallels between normal development and tumor progression. *J. Mammary Gland Biol. Neoplasia.* 15:117–134. https://doi.org/10.1007/s10911-010-9178-9

Morgner, J., L. Bornes, K. Hahn, C. López-Iglesias, L. Kroese, C.E.J. Pritchard, C. Vennin, P.J. Peters, I. Huijbers, and J. van Rheenen. 2023. A Lamb1Dendra2 mouse model identifies basement-membrane-producing origins and dynamics in PyMT breast tumors. *Dev. Cell.* 58:535–549.e5. https://doi.org/10.1016/j.devcel.2023.02.017

Morin, X., R. Daneman, M. Zavortink, and W. Chia. 2001. A protein trap strategy to detect GFP-tagged proteins expressed from their endogenous loci in Drosophila. *Proc. Natl. Acad. Sci. USA.* 98:15050–15055. https://doi.org/10.1073/pnas.261408198

Morrissey, M.A., and D.R. Sherwood. 2015. An active role for basement membrane assembly and modification in tissue sculpting. *J. Cell Sci.* 128:1661–1668. https://doi.org/10.1242/jcs.168021

Morrissey, M.A., R. Jayadev, G.R. Miley, C.A. Blebea, Q. Chi, S. Ihara, and D.R. Sherwood. 2016. SPARC promotes cell invasion in vivo by decreasing type IV collagen levels in the basement membrane. *PLoS Genet.* 12: e1005905. https://doi.org/10.1371/journal.pgen.1005905

Murray, L.S., Y. Lu, A. Taggart, N. Van Regemorter, C. Vilain, M. Abramowicz, K.E. Kadler, and T. Van Agtmael. 2014. Chemical chaperone treatment reduces intracellular accumulation of mutant collagen IV and ameliorates the cellular phenotype of a COL4A2 mutation that causes haemorrhagic stroke. *Hum. Mol. Genet.* 23:283–292. https://doi.org/10.1093/hmg/ddt418

Nakaya, Y., and G. Sheng. 2013. EMT in developmental morphogenesis. *Cancer Lett.* 341:9–15. https://doi.org/10.1016/j.canlet.2013.02.037

Netzer, K.-O., K. Suzuki, Y. Itoh, B.G. Hudson, and R.G. Khalifah. 1998. Comparative analysis of the noncollagenous NC1 domain of type IV collagen: Identification of structural features important for assembly, function, and pathogenesis. *Protein Sci.* 7:1340–1351. https://doi.org/10.1002/pro.5560070610

Özbek, S., P.G. Balasubramanian, R. Chiquet-Ehrismann, R.P. Tucker, and J.C. Adams. 2010. The evolution of extracellular matrix. *Mol. Biol. Cell.* 21: 4300–4305. https://doi.org/10.1091/mbc.e10-03-0251

Page-Mccaw, A. 2008. Remodeling the model organism: Matrix metalloproteinase functions in invertebrates. *Semi. Cell Dev. Biol.* 19:14–23. https://doi.org/10.1016/j.semcdb.2007.06.004

Page-McCaw, A., A.J. Ewald, and Z. Werb. 2007. Matrix metalloproteinases and the regulation of tissue remodelling. *Nat. Rev. Mol. Cell Biol.* 8: 221–233. https://doi.org/10.1038/nrm2125

PaulssonM. 1992. Basement membrane proteins: Structure, assembly, and cellular interactions. *Crit. Rev. Biochem. Mol. Biol.* 27:93–127. https://doi.org/10.3109/10409239209082560

Pöschl, E., U. Schlötzer-Schrehardt, B. Brachvogel, K. Saito, Y. Ninomiya, and U. Mayer. 2004. Collagen IV is essential for basement membrane

stability but dispensable for initiation of its assembly during early development. *Development.* 131:1619–1628. https://doi.org/10.1242/dev.01037

Pozzi, A., P.D. Yurchenco, and R.V. Iozzo. 2017. The nature and biology of basement membranes. *Matrix Biol.* 57-58:1–11. https://doi.org/10.1016/j.matbio.2016.12.009

Ramos-Lewis, W., and A. Page-McCaw. 2019. Basement membrane mechanics shape development: Lessons from the fly. *Matrix Biol.* 75–76: 72–81. https://doi.org/10.1016/j.matbio.2018.04.004

Randles, M.J., M.J. Humphries, and R. Lennon. 2017. Proteomic definitions of basement membrane composition in health and disease. *Matrix Biol.* 57–58:12–28. https://doi.org/10.1016/j.matbio.2016.08.006

Ratzinger, G., P. Stoitzner, S. Ebner, M.B. Lutz, G.T. Layton, C. Rainer, R.M. Senior, J.M. Shipley, P. Fritsch, G. Schuler, and N. Romani. 2002. Matrix metalloproteinases 9 and 2 are necessary for the migration of Langerhans cells and dermal dendritic cells from human and murine skin. *J. Immunol.* 168:4361–4371. https://doi.org/10.4049/jimmunol.168.9.4361

Rei, K., T. Hiroaki, D. Sheng, F. Yasuyuki, and T. Yoichiro. 2021. Tumor-cell invasion initiates at invasion hotspots, an epithelial tissue-intrinsic microenvironment. *bioRxiv.* https://doi.org/10.1101/2021.09.28.462102 (Preprint posted September 28, 2021).

Sauter, B., D. Foedinger, B. Sterniczky, K. Wolff, and K. Rappersberger. 1998. Immunoelectron microscopic characterization of human dermal lymphatic microvascular endothelial cells. Differential expression of CD31, CD34, and type IV collagen with lymphatic endothelial cells vs blood capillary endothelial cells in normal human skin, lymphangioma, and hemangioma in situ. *J. Histochem. Cytochem.* 46:165–176. https://doi.org/10.1177/002215549804600205

Schindler, A.J., and D.R. Sherwood. 2013. Morphogenesis of the caenorhabditis elegans vulva. *Wiley Interdiscip. Rev. Dev. Biol.* 2:75–95. https://doi.org/10.1002/wdev.87

Schwarzbauer, J. 1999. Basement membranes: Putting up the barriers. *Curr. Biol.* 9:R242–R244. https://doi.org/10.1016/S0960-9822(99)80153-5

Sekiguchi, R., and K.M. Yamada. 2018a. Basement membranes in development and disease. *Curr. Top. Dev. Biol.* 130:143–191. https://doi.org/10.1016/bs.ctdb.2018.02.005

Sekiguchi, R., and K.M. Yamada. 2018b. Chapter four - basement membranes in development and disease. *In* Current Topics in Developmental Biology. E.S. Litscher and P.M. Wassarman, editors. Academic Press, San Diego.

Shaw, L., R.L. Williams, and K.J. Hamill. 2020. CRISPR-Cas9-mediated labelling of the C-terminus of human laminin β1 leads to secretion inhibition. *BMC Res. Notes.* 13:90. https://doi.org/10.1186/s13104-020-04956-z

Sherwood, D.R. 2021. Basement membrane remodeling guides cell migration and cell morphogenesis during development. *Curr. Opin. Cell Biol.* 72: 19–27. https://doi.org/10.1016/j.ceb.2021.04.003

Sherwood, D.R., and P.W. Sternberg. 2003. Anchor cell invasion into the vulval epithelium in C. elegans. *Dev. Cell.* 5:21–31. https://doi.org/10.1016/S1534-5807(03)00168-0

Spurlin, J.W., III, M.J. Siedlik, B.A. Nerger, M.-F. Pang, S. Jayaraman, R. Zhang, and C.M. Nelson. 2019. Mesenchymal proteases and tissue fluidity remodel the extracellular matrix during airway epithelial branching in the embryonic avian lung. *Development.* 146:dev175257. https://doi.org/10.1242/dev.175257

Stanley, J.R., D.T. Woodley, S.I. Katz, and G.R. Martin. 1982. Structure and function of basement membrane. *J. Invest. Dermatol.* 79:69s–72s. https://doi.org/10.1111/1523-1747.ep12545830

Suzuki, K., and K. Takahashi. 2003. Reduced cell adhesion during mitosis by threonine phosphorylation of β1 integrin. *J. Cell. Physiol.* 197:297–305. https://doi.org/10.1002/jcp.10354

Sztal, T., S. Berger, P.D. Currie, and T.E. Hall. 2011. Characterization of the laminin gene family and evolution in zebrafish. *Dev. Dyn.* 240:422–431. https://doi.org/10.1002/dvdy.22537

Tamori, Y., E. Suzuki, and W.-M. Deng. 2016. Epithelial tumors originate in tumor hotspots, a tissue-intrinsic microenvironment. *PLoS Biol.* 14: e1002537. https://doi.org/10.1371/journal.pbio.1002537

Timpl, R. 1989. Structure and biological activity of basement membrane proteins. *Eur. J. Biochem.* 180:487–502. https://doi.org/10.1111/j.1432-1033.1989.tb14673.x

Timpl, R. 1996. Macromolecular organization of basement membranes. *Curr. Opin. Cell Biol.* 8:618–624. https://doi.org/10.1016/S0955-0674(96)80102-5

Töpfer, U. 2023. Basement membrane dynamics and mechanics in tissue morphogenesis. *Biol. Open.* 12:12. https://doi.org/10.1242/bio.059980

Van De Bor, V., V. Loreau, M. Malbouyres, D. Cerezo, A. Placenti, F. Ruggiero, and S. Noselli. 2021. A dynamic and mosaic basement membrane controls cell intercalation in Drosophila ovaries. *Development*. 148: dev195511. https://doi.org/10.1242/dev.195511

Walma, D.A.C., and K.M. Yamada. 2020. The extracellular matrix in development. *Development*. 147:dev175596. https://doi.org/10.1242/dev.175596

Wang, S., R. Sekiguchi, W.P. Daley, and K.M. Yamada. 2017. Patterned cell and matrix dynamics in branching morphogenesis. *J. Cell Biol*. 216: 559–570. https://doi.org/10.1083/jcb.201610048

Wei, S.C., L. Fattet, J.H. Tsai, Y. Guo, V.H. Pai, H.E. Majeski, A.C. Chen, R.L. Sah, S.S. Taylor, A.J. Engler, and J. Yang. 2015. Matrix stiffness drives epithelial-mesenchymal transition and tumour metastasis through a TWIST1-G3BP2 mechanotransduction pathway. *Nat. Cell Biol*. 17: 678–688. https://doi.org/10.1038/ncb3157

Yamaguchi, N., Z. Zhang, T. Schneider, B. Wang, D. Panozzo, and H. Knaut. 2022. Rear traction forces drive adherent tissue migration in vivo. *Nat. Cell Biol*. 24:194–204. https://doi.org/10.1038/s41556-022-00844-9

Yamakita, Y., G. Totsukawa, S. Yamashiro, D. Fry, X. Zhang, S.K. Hanks, and F. Matsumura. 1999. Dissociation of FAK/p130(CAS)/c-Src complex during mitosis: Role of mitosis-specific serine phosphorylation of FAK. *J. Cell Biol*. 144:315–324. https://doi.org/10.1083/jcb.144.2.315

Yasunaga, K., T. Kanamori, R. Morikawa, E. Suzuki, and K. Emoto. 2010. Dendrite reshaping of adult Drosophila sensory neurons requires matrix metalloproteinase-mediated modification of the basement membranes. *Dev. Cell*. 18:621–632. https://doi.org/10.1016/j.devcel.2010.02.010

Yurchenco, P.D. 2011. Basement membranes: Cell scaffoldings and signaling platforms. *Cold Spring Harb. Perspect. Biol*. 3:a004911. https://doi.org/10.1101/cshperspect.a004911

Yurchenco, P.D., P.S. Amenta, and B.L. Patton. 2004. Basement membrane assembly, stability and activities observed through a developmental lens. *Matrix Biol*. 22:521–538. https://doi.org/10.1016/j.matbio.2003.10.006

Zorina, A., V. Zorin, A. Isaev, D. Kudlay, M. Vasileva, and P. Kopnin. 2023. Dermal fibroblasts as the main target for skin anti-age correction using a combination of regenerative medicine methods. *Curr. Issues Mol. Biol*. 45:3829–3847. https://doi.org/10.3390/cimb45050247
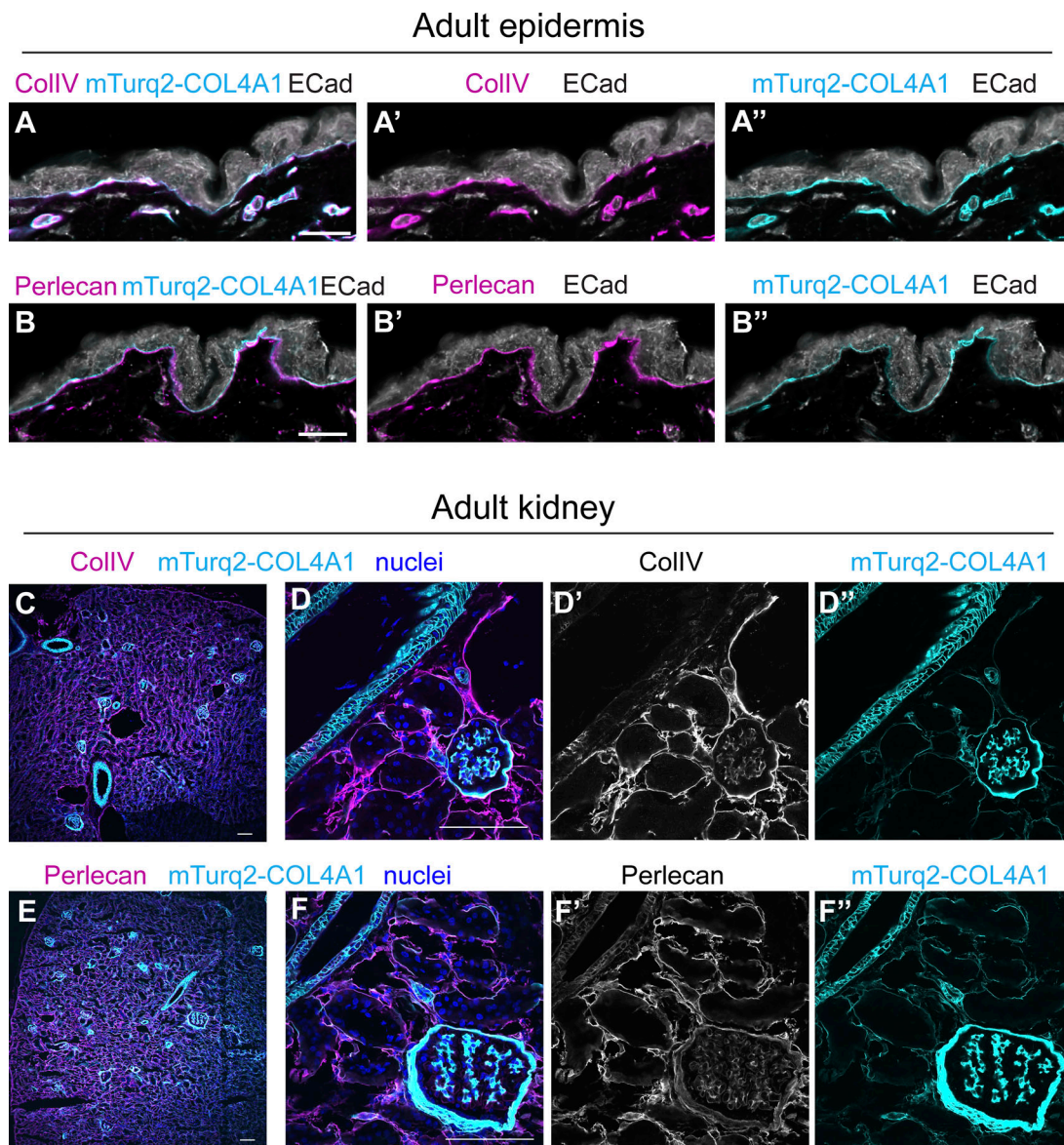
Figure S1. **Related to** Fig. 1. ***mTurq2-Col4a1* basement membrane localization in adult epidermis and kidney. (A–F)** Additional representative images from a second biological replicate *mTurq2-Col4a1/+* adult mouse. **(A and B)** Dorsal skin sections from *mTurq2-Col4a1/+* adult mouse labeled with ColIV (A and A'; magenta) or Perlecan (B and B', magenta) and E-Cadherin (grayscale). mTurq2-COL4A1 (cyan) localizes to the basement membrane underlying the interfollicular epidermis and the dermal vasculature. Scale bars, 20 μm. **(C)** Additional biological replicate of kidney sections from *mTurq2-Col4a1/+* adult mouse labeled with ColIV antibodies (magenta) and Hoechst to mark nuclei (blue). Scale bar, 100 μm. **(D–D")** High magnification view of mTurq2-COL4A1 (cyan) localization in the kidney of second biological replicate *mTurq2-Col4a1/+* adult mouse labeled with ColIV (magenta in D; grayscale in D') Hoechst (blue). Scale bar, 100 μm. **(E)** Kidney section from *mTurq2-Col4a1/+* adult mouse labeled with Perlecan antibodies (magenta) and Hoechst (blue). Scale bar, 100 μm. **(F–F")** High magnification view of mTurq2-COL4A1 (cyan) localization in the kidney of *mTurq2-Col4a1/+* adult mouse labeled with Perlecan (magenta in F; grayscale in F') Hoechst (blue). Scale bar, 100 μm.

E18.5

WT

A replicate 2

B replicate 3

SC
GL
SL
BL
De

mTurq2-Col4a1/+

C replicate 2

D replicate 3

SC
GL
SL
BL
De

E replicate 2

HD
←PM
BM

F replicate 3

HD
←PM
BM

G replicate 2

HD
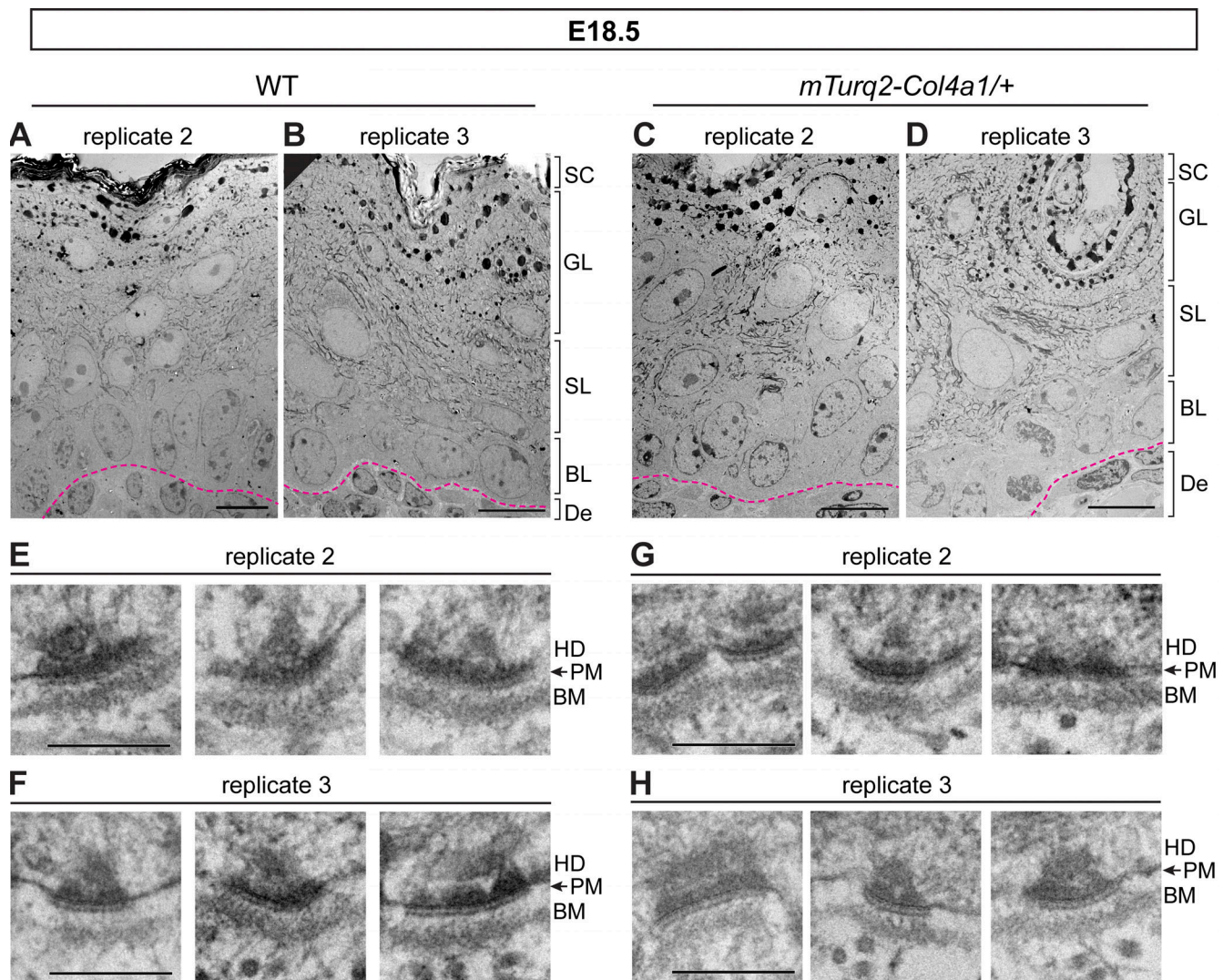←PM
BM

H replicate 3

HD
←PM
BM

Figure S2. **Related to** Fig. 3. **Ultrastructural organization of the epidermis and dermal–epidermal junction in *mTurq2-Col4a1/+* embryonic skin. (A–D)** Representative TEM images from additional experimental replicates of E18.5 WT control (A and B) and *mTurq2-Col4a1/+* (C and D) embryonic skin. Der = dermis, BL = basal layer, SL = spinous layer, GL = granular layer, SC = stratum corneum. The dotted line denotes dermal–epidermal boundary. Scale bars, 10 μm. **(E–H)** Representative images of individual hemidesmosomes at the dermal–epidermal junction region of WT control (E and F) and *mTurq2-Col4a1/+* (G and H) embryonic skin. HD = hemidesmosome, PM = plasma membrane, BM = basement membrane. Scale bars, 250 nm.
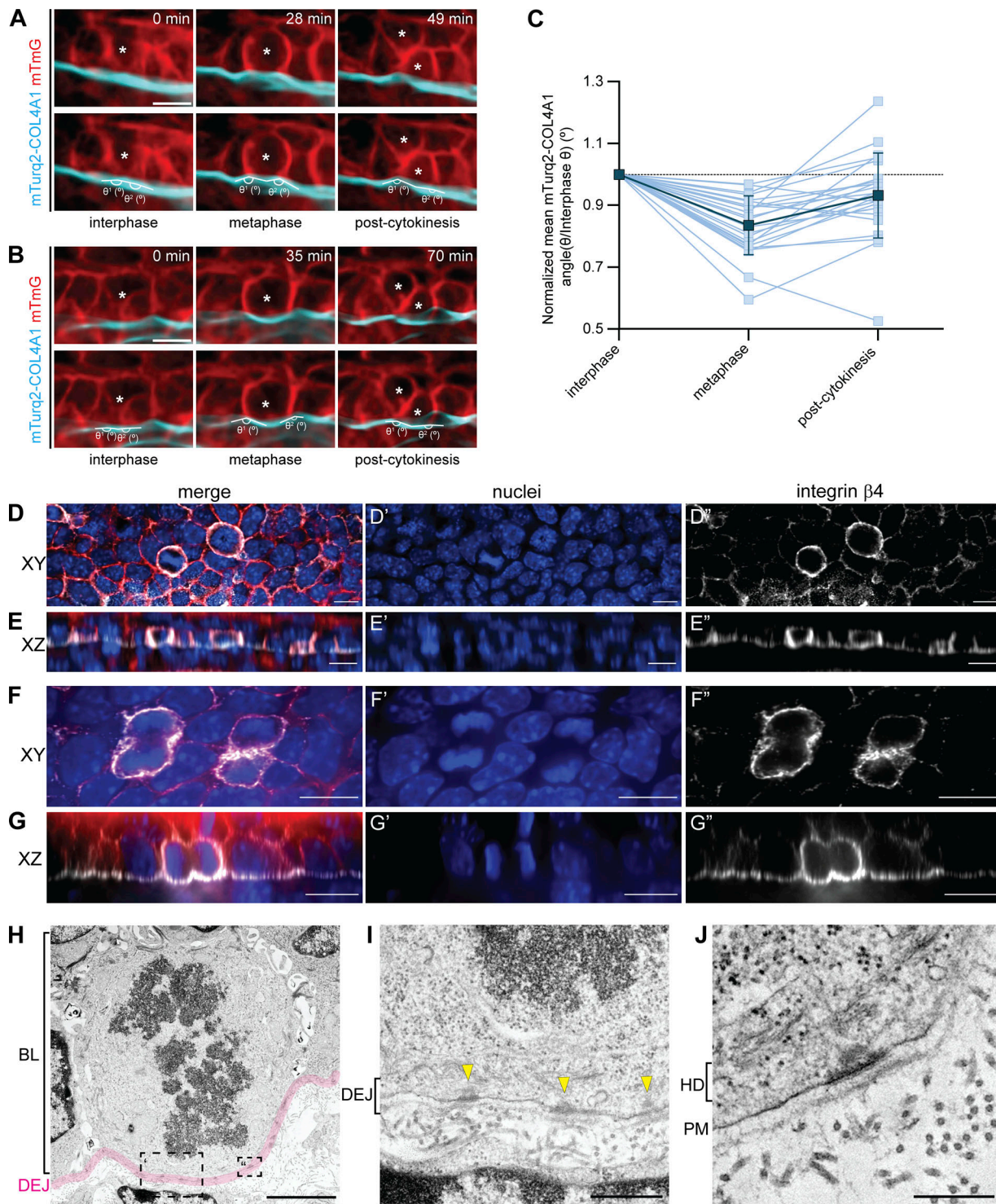
Figure S3. **Related to Fig. 5. The epidermal BM deforms around dividing basal progenitor cells. (A)** Additional example of snapshots taken from time-lapse live imaging movie of basal cell division in E15.5 *mTurq2-Col4a1/+;mTmG/mTmG* backskin. Interphase, metaphase, and post-cytokinesis stages are shown (left to right). Bottom panel shows same images with membrane curvature measurements shown. Scale bar, 10 μm. **(B)** Additional example as A. **(C)** Quantification of the average angle of BM deformation as shown in Fig. 5 F. Data is normalized to the interphase angle for each individual dividing cell. Each line represents one dividing cell. Dark blue line represents the average of all dividing cell lines. *n* = 23 dividing cells. Error bars = mean + SD. **(D)** Average intensity projection of backskin from *mTmG/mTmG* E16.5 embryo labeled with Hoechst (merge, D') and anti-β4 integrin antibody (merge, D"). **(E–E")** Average intensity projection (XZ optical reconstruction) of the image shown in D. **(F and G)** As D and E, except showing an image taken at 4× zoom. Scale bars, 10 μm. **(H–J)** Representative TEM images from E18.5 *mTurq2-Col4a1/+* embryonic skin showing a dividing basal progenitor cell maintaining hemidesmosome adhesions with the BM during mitotic rounding. BL = basal layer, DEJ = dermal-epidermal junction, HD = hemidesmosome, PM = plasma membrane. Dotted boxes (') and (") in H denote regions magnified in I and J, respectively. Scale bars, 2 μm (H), 100 nm (I), 50 nm (J).

Video 1. **Three representative time-lapse live imaging movies of hair follicles invaginating in E14.5 and E15.5 *mTurq2-Col4a1/+;mTmG/mTmG* backskins (as shown in** Fig. 5 C**).** The top panel shows the mTurq2-COL4A1 and tdTomato channels, the bottom panel shows the mTurq2-COL4A1 channel only. Scale bar, 50 µm. *t* = 343 min, 10 fps, ~70 min/sec playback speed.

Video 2. **Three representative time-lapse live imaging movies of basal progenitor cell divisions in E14.5 and E15.5 *mTurq2-Col4a1/+;mTmG/mTmG* backskins.** The top panel shows the mTurq2-COL4A1 and tdTomato channels, the bottom panel shows the mTurq2-COL4A1 channel only. Scale bar, 50 µm. *t* = 70 min, 3 fps, 21 min/sec playback speed.

Video 3. **Z-stack movie through E15.5 *mTurq2-Col4a1/+* backskin from basal layer (basement membrane) to the dermis.** Note brightly labeled blood vessels in the dermis.

Provided online are Table S1 and Table S2. Table S1 lists sgRNA and oligonucleotide sequences. Table S2 lists the primary antibodies used in this study.